

Part I

The fragmented model and its evolution

CHAPTER 2

The Hubble-Lemaître fragmented model: analytical approach

In this chapter we introduce the Hubble-Lemaître model, derive the equations governing the expansion and perform a perturbation analysis to investigate the growth of idealized overdensities.

Contents

2.1	How to build a Hubble-Lemaître model	35
2.1.1	Initial state	35
2.1.2	Fragmentation	36
2.2	The growth of overdensities: analytical study	38
2.2.1	Working equations	38
2.2.2	Linear density perturbation	40
2.2.3	Consistent initial conditions	41
2.2.4	Segregation time-scale	42
2.2.5	Example with $N = 15000$	44
2.3	Concluding remarks	45

2.1 How to build a Hubble-Lemaître model

2.1.1 Initial state

The first step to obtain a HL-fragmented model is to build an uniform sphere model. The N stars, depending on the required membership, have to be distributed randomly in space inside a certain radius, producing an uniform density. This can be achieved by sampling separately the distance to the center and the angular position of each star, in a method analog as used in [Aarseth, Hénon & Wielen \(1974\)](#) for a Plummer model. The distance to the center should be sampled from the function:

$$f_R(X) = R_0 X^2 \quad (2.1)$$

With R_0 the bounding radius and X a random variable following a uniform probability law between 0 and 1. A direct uniform law for the radius would overpopulate the outer regions. The angles ϕ and θ , respectively azimuthal and polar angle in the physics convention, should be sampled from:

$$f_\phi(X_1) = 2\pi X_1 \quad (2.2)$$

$$f_\theta(X_2) = \arccos(X_2) \quad (2.3)$$

With X_1 following a uniform probability law between 0 and 1 and X_2 between -1 and 1. The cartesian coordinates are then found:

$$x = R \sin \theta \cos \phi \quad (2.4)$$

$$y = R \sin \theta \sin \phi \quad (2.5)$$

$$z = R \cos \theta \quad (2.6)$$

$$(2.7)$$

The N particles are then homogeneously distributed in space in a sphere of radius R_0 . The next step is to attribute velocities. Unlike other models like the Plummer model, the velocities are here straightforward. We use the Hubble-Lemaître velocity field of neighbouring galaxies: velocities are radial from the Milky Way, larger with increasing distances, taking the form:

$$\mathbf{v} = H_0 \mathbf{r}, \quad (2.8)$$

with H_0 being an equivalent of the well-known Hubble parameter. For historical accuracy, I added the name of Georges Lemaître when I named my model. It has now been shown that the astronomical observations of redshifted galaxies and its interpretation as the consequence of an expanding universe predated Hubble's paper (Hubble, 1929). Georges Lemaître had published his conclusion on an expanding universe two years earlier (Lemaître, 1927). The account of this can be found in Kragh & Smith (2003); van den Bergh (2011) and Freeman et al. (2015).

An appropriate H_0 to obtain a fragmented subvirial model has to be inferior to $\sqrt{2}$ (see next section). The model obtained from this is then evolved through a nbody integrator, which in this case is NBODY6.

2.1.2 Fragmentation

The cluster expands, driven by the initial Hubble-Lemaître velocity field. During this expansion, poissonian fluctuation in density from the uniform model starts to grow: parts of the cluster with more mass initially attract more stars, forming clumps, clumps merge, spontaneously building substructure. These clumps will be analyzed in another section. If the system is bound, the expansion stops at some point, the apex, at which the initial kinetic energy has been spent and converted to potential energy: the cluster is now larger, substructured and subvirial, about to collapse. The apex time t_a of the end of the expansion and the critical value of H_0 can be derived from Newton's second law applied to an expanding spherical shell of matter.

We start from a uniform sphere of radius R_0 , total mass M . We consider spherical shells as mass elements, situated at distance r from the origin. As previously said, they are attributed a radial velocity following (for the shell at $r = R_0$) $\mathbf{v}_0 = H_0 \mathbf{R}_0 = H_0 R_0 \mathbf{u}_r$. We want to follow the radial motion of the last shell of mass m , situated at R from the origin. Newton's second law gives:

$$m \frac{dv}{dt} = -\frac{GMm}{R^2} \quad (2.9)$$

By multiplying on both sides by v and integrating between a given time and $t = 0$, one finds

$$v^2(t) - v_0^2 = 2GM \left(\frac{1}{R} - \frac{1}{R_0} \right). \quad (2.10)$$

We take $\nu = v/v_0$, $x = R/R_0$ and define:

$$E_* = \frac{2GM}{R_0 v_0^2} \quad (2.11)$$

which is a dimensionless measure of the total energy of the system. It comes

$$\nu^2 = 1 + E_* \left(\frac{1}{x} - 1 \right). \quad (2.12)$$

The evolution of the system has 3 outcomes, depending on the value of E_* :

- $E_* < 1$ The velocity is always strictly positive as the system expands ($x \rightarrow \infty$). The system is unbound.
- $E_* = 1$ The velocity approaches zero as the system expands. The expansion "stops at an infinite radius". The system is marginally bound.
- $E_* > 1$ The velocity reaches zero for a finite radius, the system is bound and will collapse back on itself once the expansion stops.

Using Hénon units, $G = 1$ and $M = 1$, and we choose $R_0 = 1$. Which gives a critical value E_* to have a bound system: $E_* = \frac{2}{H_0^2} < 1$. This means to have a bound system, which stops expanding at some point, one must have $H_0 < \sqrt{2}$. We only consider in the following the case in which $E_* < 1$. We have the expression

$$\nu = \sqrt{1 + E_* \left(\frac{1}{x} - 1 \right)} \quad (2.13)$$

which, when derived over time gives

$$\frac{d\nu}{dt} = -\frac{E_*}{2x^2} \left[1 + E_* \left(\frac{1}{x} - 1 \right) \right]^{-\frac{1}{2}} \frac{dx}{dt}. \quad (2.14)$$

Combining this with (2.9), one obtains

$$\frac{dx}{dt} = H_0 \sqrt{1 + E_* \left(\frac{1}{x} - 1 \right)} \quad (2.15)$$

which can be rewritten, using $\tilde{H}_0 = H_0 \sqrt{E_* - 1}$ and $x_t = \frac{E_*}{E_* - 1}$,

$$\frac{dx}{dt} = \tilde{H}_0 \sqrt{\frac{x_t}{x} - 1}, \quad (2.16)$$

x_a being the extent of the maximum expansion as we assumed a bound system. The subscript a is for apex. If we choose the notation $u = \frac{x}{x_a}$:

$$\sqrt{\frac{u}{u-1}} \frac{du}{dt} = \frac{\tilde{H}_0}{x_a} \quad (2.17)$$

We know that x varies from 1 to x_a , thus u varies from $1/x_a$ to 1. We can then make the change of variable $u = \sin^2 \theta$ and separate the variables to get

$$\sqrt{\frac{\sin^2 \theta}{1 - \sin^2 \theta}} 2 \sin \theta \cos \theta d\theta = \frac{\tilde{H}_0}{x_a} dt \quad (2.18)$$

which becomes after simplifications

$$[1 - \cos(2\theta)] d\theta = \frac{\tilde{H}_0}{x_a} dt. \quad (2.19)$$

We now integrate the expression from $t = 0$ to t , the time at which the expansion stops and x reaches x_a (which implies $u_a = 1$ and $\theta_a = \pi/2$):

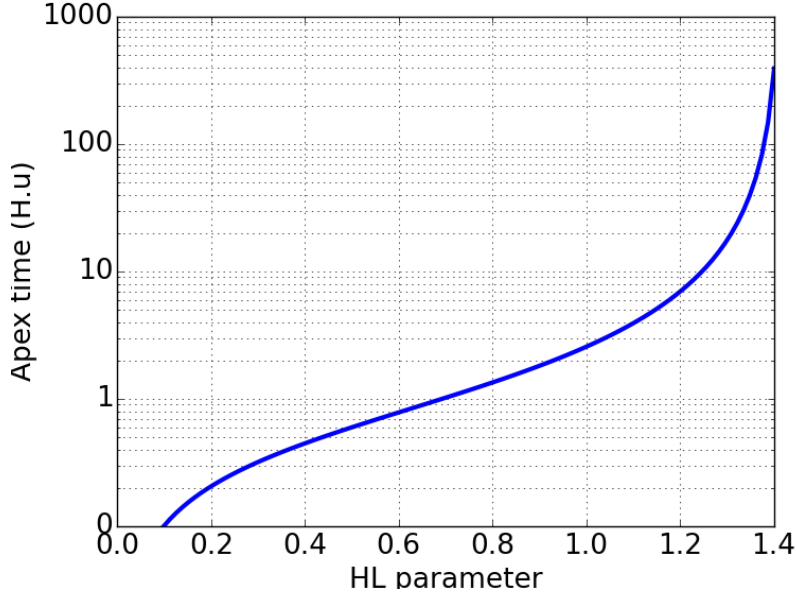


Figure 2.1: Theoretical values of the apex time, at which the system stops expanding, as a function of initial HL parameter, which tunes the strength of the initial expansion.

$$\int_{\theta_0}^{\pi/2} [1 - \cos(2\theta)] d\theta = \int_0^t \frac{\tilde{H}_0}{x_a} dt \quad (2.20)$$

$$\frac{\pi}{2} - \theta_0 + \frac{\sin(2\theta_0)}{2} = \frac{\tilde{H}_0}{x_a} t \quad (2.21)$$

$$\pi - 2\theta_0 + \frac{2}{\sqrt{x_a}} \sqrt{1 - \frac{1}{x_a}} = 2 \frac{\tilde{H}_0}{x_a} t \quad (2.22)$$

which boils down to the expression of the time at which the expansion stops:

$$t_a = \frac{E_* \left(\frac{\pi}{2} - \theta_0 \right) + \sqrt{E_* - 1}}{H_0 (E_* - 1)^{-\frac{3}{2}}}. \quad (2.23)$$

Recalling the quantities:

$$E_* = \frac{2GM}{R_0 v_0^2}; \quad x_a = \frac{E_*}{E_* - 1}; \quad \theta_0 = \sin^{-1} \left(\frac{1}{\sqrt{x_a}} \right) \quad (2.24)$$

See figure 2.1 for the value of t_a as a function of H_0

2.2 The growth of overdensities: analytical study

2.2.1 Working equations

During the expansion and in the mean-field approximation, the mass inside any shell of radius $r(t)$ is conserved as they move outwards. The position of a mass element is known in parametric form from a rescaling of its initial coordinates and we may write

$$\mathbf{r}(t) = a(t)\mathbf{x} \quad (2.25)$$

$$\mathbf{v}(t) = \dot{a}\mathbf{x} = H(t)\mathbf{r} \quad (2.26)$$

Table 2.1: Summary of main variables.

E	Total system energy
E_*	Dimensionless total energy
W	Total potential energy
E_k	Total kinetic energy
\mathcal{M}	Total system mass
R_o	Initial bounding radius
H_0	Initial Hubble parameter
v_o	Initial velocity at bounding radius
H	Variable Hubble parameter
τ	Dimensionless time
x	Comoving spatial coordinate
$a(t)$	Rescaling function
θ	Calculation angle
$\nu(\tau)$	Dimensionless velocity $1 + E_*(1/a(\tau) - 1)$
ξ	Radial displacement from comoving
$\delta\rho, \delta M, \delta\rho$	Perturbed quantities
$\mu(\tau)$	Central point mass
η	Peculiar velocity $d\xi/dt$

where \mathbf{x} is a co-moving coordinate of position, and $a(t)$ is a dimensionless function of time. The flow is homological and no shell-crossing takes place. It is convenient to introduce a dimensionless time τ such that

$$t = \frac{\tau}{H_0}. \quad (2.27)$$

We then have from equation (2.19):

$$\left[\frac{E_*}{E_* - 1} \right]^{\frac{3}{2}} [2\theta - \sin 2\theta] \Big|_{\theta_o}^{\theta} = 2\sqrt{E_*}\tau \quad (2.28)$$

with

$$a(t) \equiv \frac{\sin^2 \theta(\tau)}{\sin^2 \theta_o} \quad (2.29)$$

The dimensionless energy parameter E_* satisfies $E_* > 1$ for bound systems. The origin of time $\tau = 0$ coincides with the angle θ_o found from solving $\sin^2 \theta_o = (E_* - 1)/E_*$. The solution (2.28) provides the time-sequence for the position and velocity of any shell $0 < x < R_o$ as parametric functions of τ :

$$v(t) = H_0 x \sqrt{1 + E_* \left(\frac{1}{a(\tau)} - 1 \right)} = H_0 x \nu(\tau) \quad (2.30a)$$

$$H(t) = H_0 \frac{\nu(\tau)}{a(\tau)} \quad (2.30b)$$

$$\rho(t) = \frac{3\mathcal{M}}{4\pi R_o^3} \frac{1}{a^3(\tau)} . \quad (2.30c)$$

2.2.2 Linear density perturbation

An actual Hubble-Lemaître model will develop 3-dimensional clumps during the expansion, but to get an analytic view of this process, it is necessary to fall back on one dimension. This will shed light on the growth of clumps and help understand general trends in the system.

We follow radial density perturbations in the expanding uniform sphere described by equations (2.28) and (2.29), as the local density increase also gauges the rise in velocity dispersion. A simplified calculation for radial modes of perturbation in the linear approximation will be derived here, with the goal to determine when the clumps become mostly self-gravitating. A more detailed analysis can be found in the classic work by [Friedman & Schutz \(1978\)](#), [Peebles \(1980\)](#) and [Aarseth, Lin & Papaloizou \(1988\)](#).

We introduce a Lagrangian perturbation in the position of a shell of constant mass by substituting $\mathbf{x} \rightarrow \mathbf{x} + \boldsymbol{\xi}(\mathbf{x}, t)$ and we set $\boldsymbol{\xi} = \xi \mathbf{u}_r$ for a radial displacement. Starting from the continuity equation, a linear treatment yields an expression for the perturbed density.

$$\frac{\partial \rho}{\partial t} + \nabla(\rho \mathbf{v}) = 0 \quad (2.31)$$

which transforms into

$$\delta \rho + \nabla(\rho \mathbf{v} \delta t) = 0. \quad (2.32)$$

We make use of the equivalence:

$$\frac{\partial}{\partial r} \equiv \frac{1}{a} \frac{\partial}{\partial x} \quad (2.33)$$

to obtain, considering $\mathbf{v} \delta t = \delta \mathbf{r} = a(\tau) \boldsymbol{\xi}$ and ignoring second order terms from $\delta \rho$:

$$\delta \rho = -\nabla \cdot (a \rho \xi) = -\rho(\tau) \frac{1}{x^2} \frac{\partial}{\partial x} (x^2 \xi) \quad (2.34)$$

which leads to a perturbation in the mass integrated up to radius r

$$\delta M(< r) = \delta \left(\rho \frac{4}{3} \pi r^3 \right) \quad (2.35)$$

$$= -4\pi a^3(\tau) \rho x^2 \xi. \quad (2.36)$$

Poisson's equation in spherical symmetry gives the perturbed potential

$$\frac{1}{r^2} \frac{\partial}{\partial r} r^2 \frac{\partial}{\partial r} \delta \phi = \frac{1}{a^2} \frac{1}{x^2} \frac{\partial}{\partial x} x^2 \frac{\partial}{\partial x} \delta \phi = 4\pi G \delta \rho. \quad (2.37)$$

Substituting for $\delta \rho$ from (2.34) in (2.37), and using (2.33), we obtain:

$$\frac{\partial}{\partial x} \left(x^2 \frac{\partial \delta \phi}{\partial x} \right) = -4\pi a^2 G \rho_0 \frac{\partial}{\partial x} (x^2 \xi). \quad (2.38)$$

Integrating once, we obtain the general solution

$$a(\tau) \nabla \delta \phi = \frac{3G\mathcal{M}}{R_o^3} \left(-\xi + R_o^3 \frac{\mu(\tau)}{x^2} \right) \quad (2.39)$$

where μ stands for a central point mass. A point mass would form by shell crossing at the center of coordinates. In an expanding system, shell crossing at the center is unlikely. For that reason, we make $\mu = 0$ in the remainder of this paper.

The equations of motion at co-moving radius $x + \xi(x, t)$ can be expanded to first order in ξ ; identifying terms of the same order we obtain (with $\partial/\partial x = \nabla_x$)

$$a(\tau) \frac{d^2}{dt^2} \xi + 2\dot{a}(\tau) \frac{d}{dt} \xi = -\nabla \delta \phi - \xi \nabla_x \nabla \phi - \ddot{a}(\tau) \xi. \quad (2.40)$$

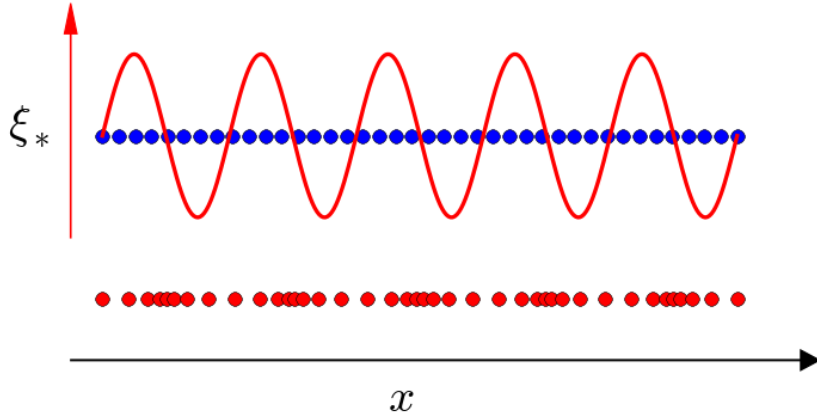


Figure 2.2: Schematic illustration of a sinewave density perturbation (red line) applied to an uniform distribution of matter (blue dots) and the resulting distribution (red dots). The mode displayed here has $m = 10$ and its amplitude was exaggerated.

The second and third terms on the right-hand side cancel out exactly ; the first is known from (2.39). It is standard practice to demote this second-order dynamical equation to a set of first order equations ; for convenience we use the initial system radius R_o as unit of length, and we introduce starred (*) dimensionless variables. We then have $x = R_o x_*$, $\xi = R_o \xi_*$, and so on. After simplification using the dimensionless functions of τ defined in (2.27) and recalling that $\dot{a}(\tau) = H(\tau)$, the differential equations read

$$\frac{d}{d\tau} \xi_* = \eta_*(\tau) \quad (2.41a)$$

$$\frac{d}{d\tau} \eta_* = \frac{3E_*}{a(\tau)^2} \xi_* - 2 \frac{H(\tau)}{a(\tau)} \eta_* \quad (2.41b)$$

where we have introduced the peculiar velocity $\eta \equiv d\xi/dt = H_0 R_o \eta_*$.

2.2.3 Consistent initial conditions

Initial conditions

Equations (2.41) can be numerically integrated with an explicit integration scheme once the initial values R_o, H_0, \mathcal{M} and $\xi_*(0)$ are specified and values of $a(\tau)$ are obtained from (2.29) and (2.28). All functions of the dimensionless time τ are set to unity except that $\eta_*(0) = 0$. The solution is shown in the next section, on Fig 2.3a.

The Hubble parameter $H(\tau) \rightarrow 0$ when the system reaches a maximum radius $a(\tau)R_o$ ($\theta[\tau] = \pi/2$ in Eq. 2.29). Around that time, equation (2.41b) transforms so the Lagrangian displacement ξ_* grows exponentially, and the clumps become the densest. We investigate the growth of a density perturbation as a Fourier fragmentation mode before that. In the linear regime, such a mode is decoupled from all the others. We pick

$$\xi_*(x, 0) = \xi_*^{(o)} \sin(kx), \quad (2.42)$$

where the wavenumber k is such that $kR_o = m\pi$ and $\xi_*(R_o, 0) = \xi_*(R_o, \tau) = 0$ at all times. When deciding which wavenumber to choose, we must bear in mind the finite numerical resolution of the models that we will present later. The next subsection gives quantitative arguments that motivated our choices. The aspect of the perturbed system is shown as a rough schematic on Fig 2.2.

Fourier modes: resolution issues

An uniform distribution of N discrete mass elements cannot resolve infinitely small wavelengths, the lower limit depends on the mean separation $l_o \simeq R_o/N^{1/3}$ which gives a reference wavelength $\lambda/R_o = \lambda_* \geq N^{-1/3}$ for a resolved Fourier mode. Since $kR_o = m\pi$, this also implies that $m \leq 2N^{1/3}$.

The initial amplitude $\xi_*^{(o)}$ of the perturbation can be tailored to the actual Poissonian fluctuations in a uniform distribution of discrete elements. The radius bounding a shell of N mass elements distributed randomly will fluctuate freely between r , $r + \delta r$ due to stochasticity. The radius r of a uniform sphere being a power-law of mass M , we find:

$$\frac{\delta r}{r} = \frac{1}{3} \frac{\delta M}{M} = \frac{1}{3} \frac{\delta N}{N} = \frac{1}{3} N^{-\frac{1}{2}} \quad (2.43)$$

for identical mass elements. We then compute the number-averaged value $\langle \delta r/r \rangle$ by summing over all elements from 1 to N and dividing by $N - 1$ to find

$$\left\langle \frac{\delta r}{r} \right\rangle = \langle \xi_*^{(o)} \rangle = \frac{2}{3} \frac{\sqrt{N} - 1}{N - 1} . \quad (2.44)$$

Thus the mean amplitude (in units of R_o) is $\langle \xi_*^{(o)} \rangle \simeq 1/10$ for $N = 32$ which drops to $\langle \xi_*^{(o)} \rangle \simeq 6 \times 10^{-4}$ when $N = 10^6$. We checked that the mode with the shortest wavelength λ_* still resolved would have a displacement $\langle \xi_*^{(o)} \rangle$ initially smaller than $\lambda_*/2$ for any sensible value of N . This in turn implies that this mode may grow over time to reach an amplitude $\xi_*(x, \tau) \simeq \lambda_*/2$, which is the point when orbit-crossing between shells of constant mass must occur. In other words, at this point, the overdensity transitions from linear convergence of particles to collisional evolution (not covered by Eqs. 2.41). The time when shell-crossing occurs can be seen as the "birth" of a clump, whether this clumps undergoes consequent two-body relaxation effects depends on its characteristics, such as density and membership, and the remaining time before the end of expansion.

2.2.4 Segregation time-scale

We already noted that H_0^{-1} sets a time-scale for the expansion of the system. That time should be chosen so that it matches the hydrodynamical star formation phase of $0.5 - 1$ Myr (Maschberger & Clarke, 2011; Bate, Tricco & Price, 2014). When $H(\tau) = 0$ and the expansion is over, the stars relax to a new equilibrium driven by star-star interactions. Therefore we need to address first the internal dynamics in clumps in time units of H_0^{-1} , before discussing the later phase of violent relaxation and consider the system as a whole. The definitions are the same, only the face values change between the two phases of evolution.

Let us consider a clump of membership N_λ initiated by a Fourier mode of wavelength λ . With its total density $\rho + \delta\rho$ given by Eq. (2.34), we may write

$$\rho_g = \frac{\rho_o}{a^3(\tau)} \left(1 + \frac{\delta\rho}{\rho} \right) \equiv \frac{\rho_o}{a^3(\tau)} \rho_*. \quad (2.45)$$

Combining this with Eqs. (1.5), (1.6) and (1.10) from the introduction, the mass-segregation timescale in the clump now reads:

$$t_{ms} = \frac{0.138}{6} \pi \left(\frac{3}{4\pi} \right)^{1/2} \frac{\langle m_* \rangle}{\max\{m_*\}} \frac{N_\lambda}{\ln 0.4 N_\lambda} (G\rho_g)^{-\frac{1}{2}} . \quad (2.46)$$

Making use of the equality

$$\frac{4\pi}{3} G\rho_o = H_0^2 E_*, \quad (2.47)$$

the last three relations simplify to the expression of the new dimensionless mass-segregation timescale:

$$\tau_{ms} = H_0 t_{ms} = \frac{0.138}{6} \pi \frac{a_\lambda^{3/2}}{(\rho_* E_*)^{1/2}} \frac{\langle m_* \rangle}{\max\{m_*\}} \frac{N_\lambda}{\ln 0.4 N_\lambda} \quad (2.48)$$

where a_λ refers to the expansion factor $a(\tau)$ evaluated at time τ when $\xi_* \simeq \lambda_*/2$. Note that our use of Eq. (2.34) to compute ρ_g means that the gravitational radius r_g does not have its usual definition based on the gravitational energy W of the system. Linking ρ_g to R_g in this way has the advantage that R_g is not derived from an implied mass profile, which is (by definition) not resolved here.

Clearly the segregation time depends strongly on the mass spectrum of individual clumps, on their membership N_λ , as well as the density contrast $\rho_*(\tau_\lambda)$. We find the density contrast from (2.42) and (2.34),

$$\left. \frac{\delta\rho}{\rho} \right|_{\tau=0} = -\frac{1}{x^2} \frac{\partial}{\partial x^2} x^2 \xi = -\left(2 \frac{\sin m\pi x_*}{m\pi x_*} + \cos m\pi x_* \right) m\pi \xi_*^{(o)}$$

which admits an upper-bound of $3m\pi\xi_*^{(o)}$. In the course of evolution, the initial amplitude of perturbation grows to $\xi_* = \lambda_*/2$ so that the density contrast peaks at

$$\rho_* = 1 + \frac{\delta\rho}{\rho} = 1 + 3m\pi\lambda_*/2 = 1 + 3\pi, \quad (2.49)$$

where the last substitution follows from the definition of the integer m . The mass M_λ in a shell bounded by $r, r + \lambda$, is known from the unperturbed density profile ; in terms of the total system mass \mathcal{M} , we find

$$\frac{M_\lambda}{\mathcal{M}} = (\overline{3x_*^2} + \lambda_*^2/4)\lambda_* = (1 + \lambda_*^2/4)\lambda_*, \quad (2.50)$$

where we have replaced $3x_*^2$ by its space-averaged value in the last step. Eq. (2.50) provides an estimate of bound mass of a clump formed through the growth of a radial perturbation mode. If all the stars have equal masses, or, if the stellar mass function is symmetric with respect to the mean value $\langle m_* \rangle$, the ratio of the number N_λ of stars in the clump to the total number N is in the same proportion as $\frac{M_\lambda}{\mathcal{M}}$. We find an estimate for N_λ which reads

$$N_\lambda = N \left(1 + \frac{\lambda_*^2}{4} \right) \lambda_*. \quad (2.51)$$

We argued in §2.3.2 that a resolved mode should have $\lambda_* \geq N^{-1/3}$, which translates as:

$$N_\lambda > N^{2/3} \left(1 + \frac{N^{-2/3}}{4} \right). \quad (2.52)$$

This number inserted into Eq.(2.48) leads to a rough picture of the segregation process in clumps. The rate of mass segregation leans on the choice of initial value for the expansion phase, H_0 . In the limit when $H_0 = 0$, there is no expansion whatsoever, and the clumps form unsegregated (aside from random associations when attributing positions and velocities to the stars) during global infall. If by contrast, the expansion is vigorous, $a_\lambda \gg 1$, and the segregation timescale remains large. For $N \sim 10^4$, we compute from (2.52) $N_\lambda \gtrsim 464$: a clump with that many stars will mass-segregate rapidly only if its stellar mass function includes very massive stars. We note that one-dimensional (radial) modes would in fact split into several smaller fragments in a three-dimensional calculation.¹ We expect the clumps to form quickly and contain $N_\lambda \ll 464$

¹ A full-grown radial mode forms a thin shell subject to fragmentation. See *e.g.* Ehlerova et al. (1997); Wünsch et al. (2010).

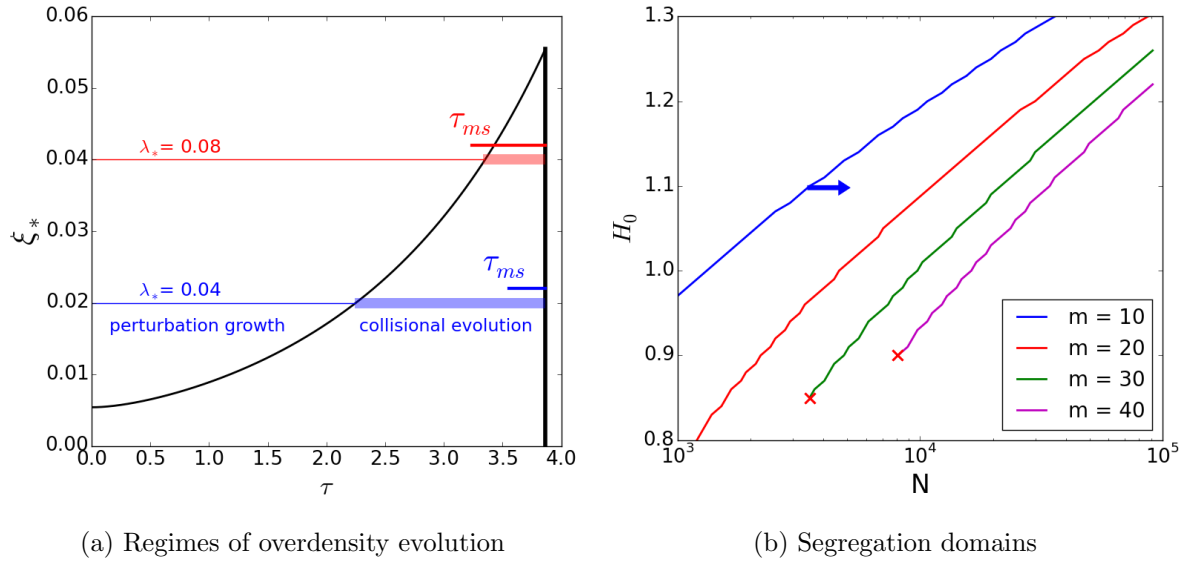


Figure 2.3: (a): growth of perturbation ξ_* over dimensionless time τ until the end of expansion at $\tau = 3.84$. An overdensity seeded with a wavelength λ_* begins its collisional evolution when ξ_* reaches $\frac{\lambda_*}{2}$. These regimes are illustrated for $\lambda_* = 0.04$ and $\lambda_* = 0.08$. The overdensities have to evolve collisionally for at least τ_{ms} to mass-segregate. This time-scale is also shown for each case. The blue case evolve collisionally for several τ_{ms} and will end up mass-segregated, while the red case visibly don't have time to segregate. Modes of large wavelength tend to produce less mass-segregated clumps. (b) for a given number of nodes m , a model on the right of the corresponding line (arrow for $m = 10$) will have mass-segregated overdensities at the end of the expansion, while on the left, the collisional evolution is too short for segregation to set in. The red crosses show the minimum N below which the modes cannot be resolved.

stars, so that the internal dynamics will drive mass segregation *before* the system expansion stops. Because this depends in the details on H_0 and other important parameters, we defer the analysis to §?? and N-body simulations.

2.2.5 Example with $N = 15000$

We now make use of all previous development to follow the evolution of a perturbation in a given system and assess its dynamical state.

To ease comparisons with N-body calculations cast in standard Hénon units, we set $\mathcal{M} = G = R_o = 1$ and use $H_0 = 1.0833 \dots \simeq 1$ so that the total binding energy $E = -1/4$, which gives a value of $E_* \simeq 6/7$. The Hubble expansion proceeds until a time $t = \tau/H_0 \simeq 3.87/H_0$, when $H = 0$ and the bounding radius R reaches $R = a(\tau)R_o \simeq 2.4R_o$. The evolution time up to that point coincides almost exactly with the *current* global system free-fall time of ≈ 4.1 time units. System-wide collapse to the barycentre will ensue on the same time-scale, but now this process will involve the merging / scattering of several high-density clumps.

For simplicity, and for ease of calculations, we chose the mass of individual stars to follow a truncated Salpeter (1955) distribution function, where the distribution function $dN/dm \propto m_*^{-\alpha}$ with index $\alpha = 2.35$ for masses in the range $0.3M_\odot < m_* < 100M_\odot$ giving a mean value of $\simeq 1M_\odot$.

We set $H_0 = 1$ and $N = 15000$ as reference². We compute a mean initial amplitude of perturbation $\xi_*^{(o)} \approx 0.005$ with a shortest-resolved wavelength $\lambda_* \approx 0.04$. Fig. 2.3a displays the solution from integrating Eqs. (2.41). The amplitude $\xi_*(\tau)$ grows monotonically and crosses

²The more accurate value is $H_0 = 1 + 1/12 = 1.0833$ but we rounded up to 1 to simplify the discussion

the values $\lambda_*/2$ at $\tau \approx 2.3$: thereafter the perturbation enters a non-linear regime of evolution during which the internal dynamics may become collisional ($\Delta\tau > \tau_{ms}$). A second case is depicted on Fig. 2.3a, where the wavelength $\lambda_* = 0.08$ and the perturbation reaches amplitude $\xi_* = \lambda_*/2$ at $\tau \approx 3.6$: there is then too little time left before the end of the Hubble expansion phase for a clump of stars to evolve collisionally ($\Delta\tau < \tau_{ms}$).

The dynamical state of individual clumps is clearly a question of membership N_λ and mass spectrum as shown in (2.48). We have been arguing that most small-size clumps will show collisional internal evolution : a small cluster of stars would lose low-mass stars in the process and so have an increased ratio of average- to maximum stellar mass. It is not clear, then, whether this trend is strong enough to compensate for the (almost) linear dependence on membership.

2.3 Concluding remarks

We presented the recipe to build a Hubble-Lemaître fragmented model. As the model is analog to the cosmological model of an expanding universe, we adopted the same notations. However, three important differences should be noted:

- Our model is limited in space.
- We expect a collisional evolution in the overdensities.
- The expansion of our model slows down over time, as there is no internal energy source akin to the cosmological Dark Energy.

With an appropriate H_0 , below $\sqrt{2}$, the expansion of our model ends at a time we named apex time. We derived its expression as a function of H_0 , as well as the governing equations of the expansion. A perturbation analysis was performed to follow idealized radial overdensities. We expect clumps to undergo a phase of linear convergence followed by collisional evolution. We can also expect mass-segregation to occur in our clumps, though quantitative prediction cannot be obtained from idealized radial shell-like overdensities. N-body simulations are needed to obtain detailed characteristics.

CHAPTER 3

Nbody application

After the previous analytical study, we present here the characteristics of numerically obtained Hubble-Lemaître fragmented models. We present a clump-finding algorithm that we use to analyse the population of clumps obtained from the expansion. The influences of N , H_0 and stellar mass functions on the clumps mass function are investigated. We then look at the stellar content and distribution inside clumps, comparing them to clumps obtained from hydrodynamical simulations.

Contents

3.1 N-body simulations	47
3.1.1 Presentation of the runs	47
3.1.2 Clump finding algorithm	49
3.2 Clump mass function	51
3.2.1 Influence of H and N	51
3.2.2 Influence of stellar mass function	54
3.3 Clump contents	56
3.3.1 The velocity field	56
3.3.2 The stellar mass function in clumps	58
3.3.3 Mass segregation	61
3.4 Concluding remarks	62

3.1 N-body simulations

3.1.1 Presentation of the runs

To investigate the influence of various parameter and to follow the dynamical evolution (see next chapter), a large set of N-body simulation of Hubble-Lemaître models was performed. They are summarised in table

We draw N stars from an Salpeter distribution function which we truncate by default to $100M_\odot$; in some calculations we will use a lower bound of $20M_\odot$, and in others we use identical masses. The integration was performed with NBODY6, which treats the gravitational forces of stars with no softening of the potential. The code preserves the total energy and angular momentum to better than one part in 10^4 for integration over ~ 100 time units.

An example of the evolution of the system is shown on Fig 3.1.

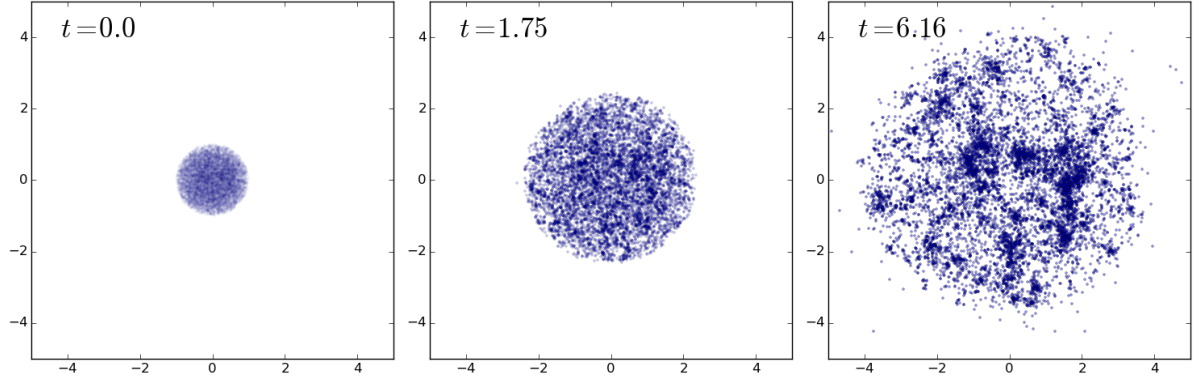


Figure 3.1: Progressive fragmentation through the Hubble expansion. The left panel shows the initial uniform sphere; the middle panel, an intermediate step, slightly fragmented with a slowed down expansion; the right panel is the final stage, when the expansion has stopped and the fragmentation is fully developed. $N=10000$ particles were used in this N-body model, with $H_0 = 1.0$. Time and coordinates are in Hénon units.

Table 3.1: Summary of fragmentation models and their characteristics. These simulations started from an uniform sphere and were stopped when the expansion halted at the apex time, t_a . The third column shows the number of independent computations for each model. Models that stops at 40 H.u set the fragmented system as initial conditons, shifting time by t_a . RunshN are detailed in the two lower tables.

Name	N	Sampling	Mass range	t_{end}	Model
RunshN	see below	175	[0.3 - 100]	t_a	Hubble
Rmh20	15000	30	[0.35- 20]	t_a	Hubble
Rmh100	15000	30	[0.3 - 100]	t_a	Hubble
Rmh1	15000	60	1.0	t_a	Hubble
R40h20	40000	1	[0.35- 20]	t_a	Hubble
R40h100	40000	1	[0.3 - 100]	t_a	Hubble
R80h100	80000	1	[0.3 - 100]	t_a	Hubble
Rh100	15000	1	[0.3 - 100]	40 H.u	Hubble
Rh20	15000	1	[0.35- 20]	40 H.u	Hubble
Ru100	15000	1	[0.3 - 100]	40 H.u	Uniform
Ru20	15000	1	[0.35- 20]	40 H.u	Uniform

Detailed characteristics of RunshN:

N	1000	2000	4000	8000	16000
Sampling	12	8	5	5	5

Each RunshN model is performed with 5 different H_0 .

H_0	0.8	0.9	1.0	1.1	1.2
-------	-----	-----	-----	-----	-----

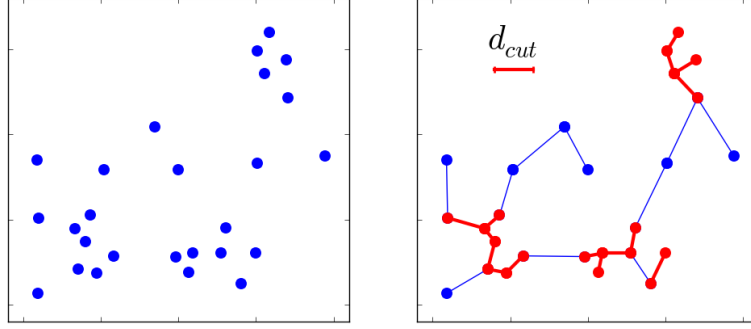


Figure 3.2: Illustration of a Minimum Spanning Tree and its use to isolate subgroups, using a cutting length d_{cut} .

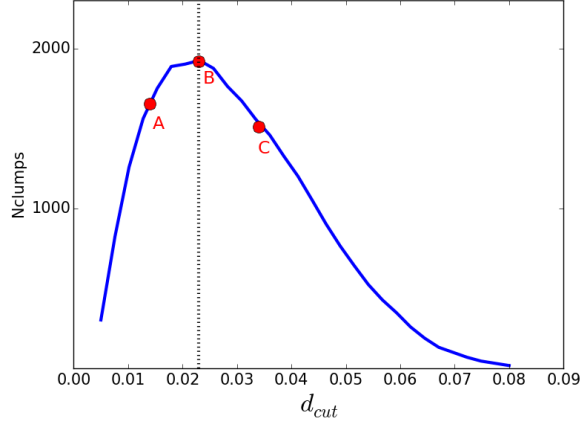
3.1.2 Clump finding algorithm

As seen on Fig 3.1, once expansion stops, the distribution is roughly spherical and visibly clumpy. By clump we mean here a local overdensity of stars. To characterize the model, it is necessary to find and isolate clumps, using an efficient clump-identification algorithm (or, *halo-finding* in cosmology). Several methods are commonly used such as the HOP algorithm (Eisenstein & Hut, 1998; Skory et al., 2010) which relies on attributing local densities to each particle and separating the clumps through density thresholds. The HOP algorithm is very robust on large cosmological data sets. However, our calculations have comparatively coarse statistics and noisy density fields. This issue, coupled with the large number of free parameters of the HOP algorithm, makes the method less appealing.

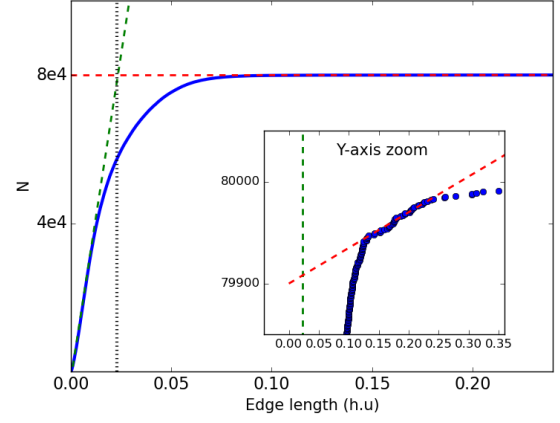
Instead we follow Maschberger et al. (2010) who adapted the minimum spanning tree (MST ; see e.g. Allison et al. 2009b; Olczak, Spurzem & Henning 2011) technique to the detection of clumps. A spanning tree is a set of edges connecting a group of particles without closed loops ; the MST seeks to minimise the total length of the edges. One may then construct the MST for the whole system, and then delete all edges larger than a chosen cutting length, d_{cut} . The sub-sets that are still connected are labeled as clumps. This process is illustrated in Fig 3.2. In practice a minimum sub-set size N_d is also chosen so as to avoid many small-N subgroups : experience led us to choose $N_d = 12$ for the minimum number of stars per clump.

With N_d fixed, the length d_{cut} is then the only free parameter left. There is some freedom in choosing an appropriate value. Maschberger et al. (2010) fixed the value of d_{cut} by visual inspection of clumps. We instead identified clumps in a fragmented system for a range of values for d_{cut} and settled for the value which optimised the number of identifications. This is shown on Fig. 3.3a for the fully-fragmented state of R80h100 (see table 3.1. For small values of d_{cut} , the number of detected clumps at first increases rapidly. The rise is due to the length d_{cut} initially being small compared with the typical volume spawned by N_d or more nearest-neighbours. Beyond a certain value, a transition to another regime occurs, whereby the algorithm starts to connect previously separated clumps, counting them as one. The number of clumps thereafter begins to decrease. The value $d_{cut} \approx 0.023$ H.u optimises the outcome of the clump-search. This is a generic feature of the MST algorithm and we have adopted the same strategy throughout, adapting the value of d_{cut} to the number N of stars used.

Another method to find the critical cutting length was used by Gutermuth et al. (2009); Kirk & Myers (2011). In these works, the authors build the MST, then trace the cumulative distribution function of all edges in the tree. In a clumpy configuration, there are at least two regimes: the "intra-clump" regime, with the majority of small edges, and the "inter-clump" regime with longer, scarcer edges. The intersection of the linear fits to these regimes provide a



(a) Number of clumps vs d_{cut}



(b) Cumulative distribution of MST edges

Figure 3.3: Two different methods to identify the critical d_{cut} for clump detection. Both methods give the same value. For this 80k model, the value is 0.023 in Hénon units. The red linear fit on (b) was made on the linear portion with sufficient data points, discarding the very few further points departing from the tendency.

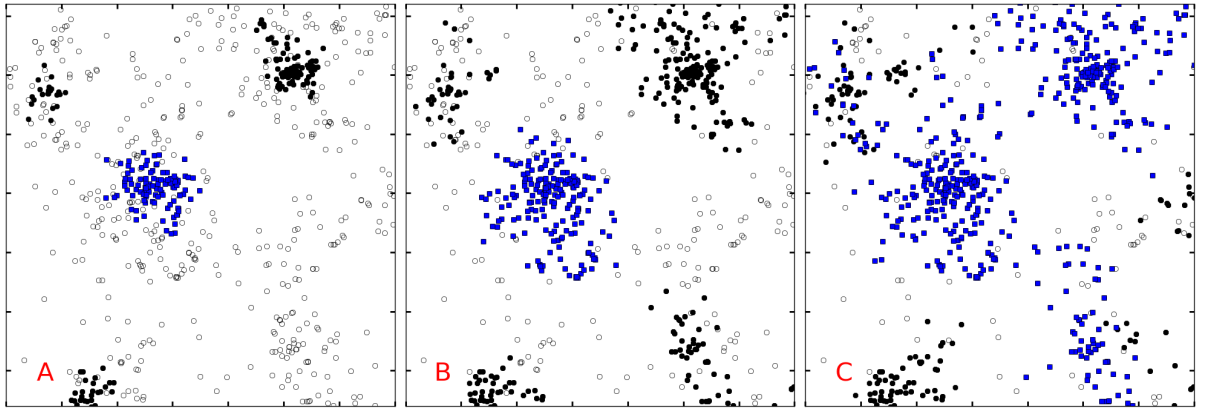


Figure 3.4: Example of detected clumps for three cutting length, 0.014 (top panel), 0.024 (middle panel), 0.034 (bottom panel), which were labeled A,B,C in Fig. 3.3a. A cube within a 80k particles fragmented model was extracted and projected. Empty circles are stars which do not belong to any clump, black circles are clump members, and blue squares are stars that are identified as a single large clump. Tick marks are spaced by 0.05 length units for a box size of 0.35 units.

good cutting length for clump detection. This procedure was applied to our system and gave the same result than the clump count, as shown on Fig 3.3b.

On Fig. 3.4, a sub-set of R80h100 is shown; we have identified stars that belong to clumps with filled symbols. The three panels on that figure are each for a different value of d_{cut} , increasing from top to bottom. For the smallest value $d_{cut}=0.013$ H.u, clumps look somewhat truncated as we are still in the under-sampling regime and only their cores registered as clumps. The second, optimal, value $d_{cut}=0.023$ H.u produces visually well-isolated clumps. Finally, the third and largest value is so that clumps begin to merge together : this is shown by the unique clump identified in the bottom panel (filled blue squares).

3.2 Clump mass function

The numerical realizations of the Hubble-Lemaître model allows to assess the influence of important parameters on the fragmentation, such as H_0 , N and the stellar mass function.

3.2.1 Influence of H and N

We wish to evaluate the influence of H_0 and N on the fragmentation and clump growth. H_0 tunes the strength of the expansion, which tunes the duration of the fragmentation. A stronger initial expansion allows for more time for clumps to grow, so we expect more massive clumps with increasing H_0 . On the other hand, a higher N smooths the spatial distribution, reducing Poisson noise in the distribution. However, a high membership only samples more stars from the same stellar mass function, and the density fluctuations should not change in nature, just scale down with the average distance between stars. We do not expect N to significantly affect the fragmentation in physical units.

To verify these, a set of simulation was performed to explore the mass function of clumps in the H_0 - N parameter space. The models have 5 different memberships that go as powers of 2 in thousands, with an increasing sampling to obtain acceptable statistics. They are summarised in table 3.1 under the name RunsHN.

Apex time

In section 2.1.2, we derived an analytical prediction for the apex time of our expanding models. To compare our numerical realizations to this prediction, we follow for each model the evolution of the half-mass radius over time, then take the apex time as the maximum radius time, when the cluster stops expanding and starts collapsing.

We show on Fig 3.5 the expected analytical curve as a dashed line, then the numerically obtained apex times from our different H_0 and memberships, averaged over all similar runs. The 16k runs follow the analytical expectation within 5%, while lower membership models take more time than expected to stop expanding at high H_0 , overshooting by as much as 30% for $H_0 = 1.2$. Visual inspection of the runs showed that low memberships were more susceptible to have a clump "take over" during the expansion. As we will show in the present section, low- N clusters contains more massive clumps in relative mass than high- N models. When a massive enough clump form during the expansion, it offsets the matter distribution and skews the half-mass radius (computed from the barycenter of the full system) to higher values, offsetting its fall from the collapse. To reduce unwanted "sur-fragmentation" effect, we use analytical apex times to select our fragmented configurations.

Clump mass function

The clump-finding algorithm was ran on the fragmented models to obtain the clump mass function. The results are summarised as histograms on figures 3.6 and 3.7. We have used bins

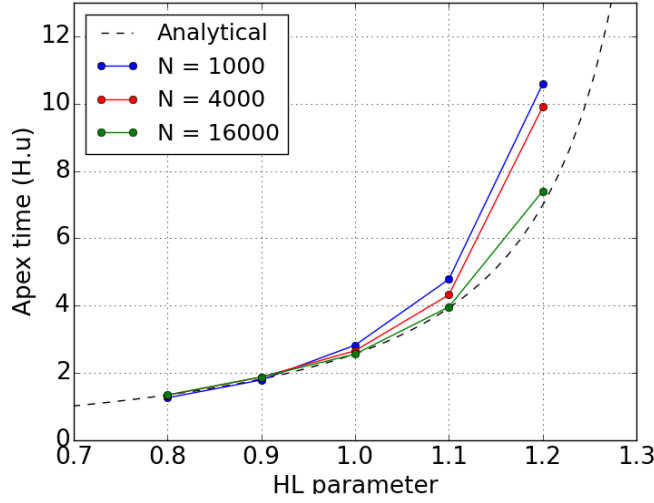


Figure 3.5: Analytical and simulated apex times as a function of H_0 .

of constant logarithmic intervals. We average the results over each model’s sampling, hence the histogram can go down to fractional values.

Looking at the top panels of Fig 3.6, we see the mass function of clumps in *relative* mass, the percentage of total mass they contain. Clumps in small-N systems tends to contain a much larger portion of the total system mass than in large-N systems, which is even clearer in the normalized count sub-panels. In fact, for $H_0 = 0.8$, the peak of the mass function for $N=1k$ happens at 1.1% of total mass, while for $N=16k$, it happens at 0.07%. These values ratio gives ~ 16 , the membership ratio: the clumps relative masses are inversely proportional to the model’s membership.

This can be interpreted as a underlying common clump distribution in physical mass, regardless of the total membership of the model. This is confirmed by looking at the bottom panels of Fig 3.6, in which clump distributions are plotted in physical mass, once the masses of stars have been rescaled from Hénon units to match the original stellar mass function. Looking at the normalized count subpanels, it is clear that 1k and 16k models have the same clump distribution, when raw count subpanels show clumps are expectedly more numerous in high-N models. The difference between $H_0 = 0.8$ and 1.2 is not clear from the graph, but it seems a higher H_0 pushes the upper limit of the distribution to slightly higher masses.

To illustrate this last trend, we turn to Fig 3.7 where clump MF are shown for various H_0 and a common membership. For both $N=1k$ and $N=16k$, the distribution preserves its shape for various H_0 , and gets prolonged at higher clump masses for $N=16k$, as more mass is available to build clumps.

Though the distribution does not undergo any dramatic change, a weak trend with H_0 is seen in both panels: as the strength of expansion increases, the distribution slightly decreases at low clump masses and slightly increases at higher clump masses, the pivot masse being $\sim 30 M_\odot$. We look at the 16k model and follow the cumulated mass inside all clumps, as well as the percentage of this mass in clumps below and above $30 M_\odot$, for different H_0 :

H_0	0.8	0.9	1.0	1.1	1.2
M_{tot}	3502	3478	3582	3683	3561
$< 30M_\odot(\%)$	66	65	55	49	44
$> 30M_\odot(\%)$	34	35	45	51	56

From this data, we get two facts about our fragmented models: the mass contained in clumps

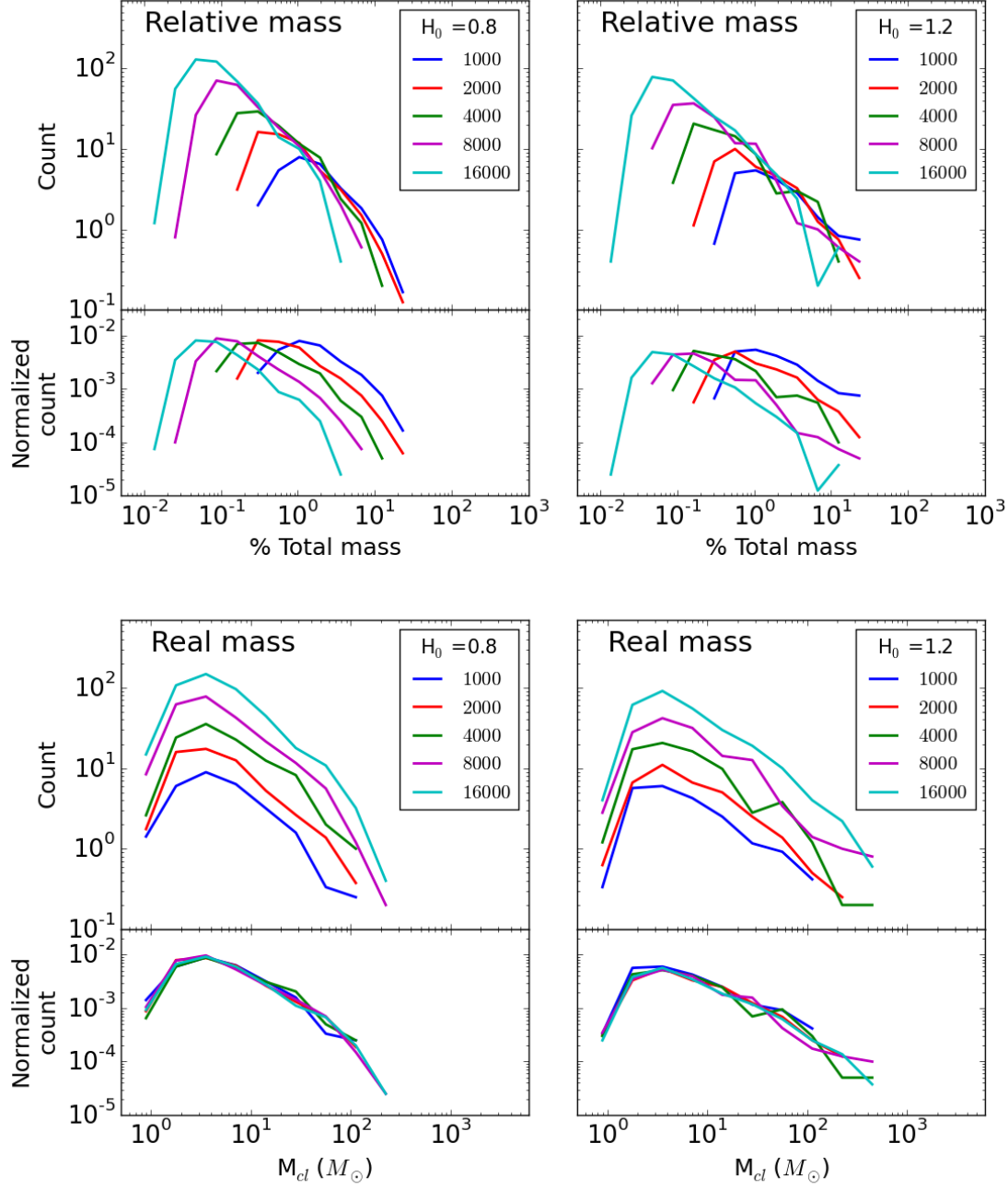


Figure 3.6: Clump mass function for several memberships and two H_0 . Masses in the top panels are in Hénon units, the x-axis was scaled with a factor 100 to get a percentage of the total mass of the system. Bottom panel masses are in physical units. In each panel, top sub-panel shows actual clump count in each bin (averaged over sampling), while bottom sub-panel normalize the count by the model membership.

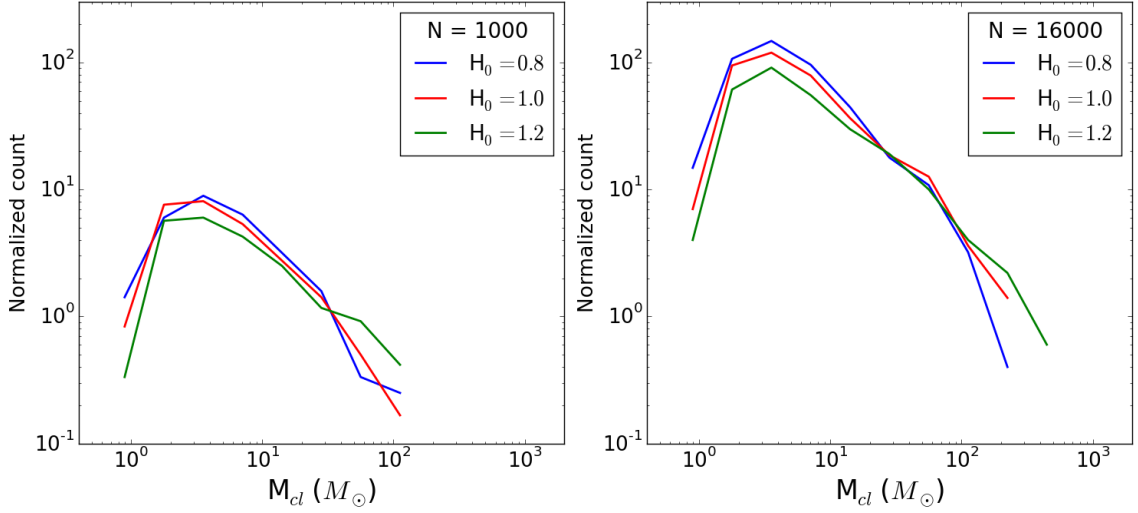


Figure 3.7: Clump mass function (real mass) for several H_0 and two memberships.

does not depend on H_0 ($<2\%$ dispersion) and there is a transfer of mass from small clumps to more massive ones as the expansion lasts longer.

To summarise: the general shape of the clump mass function is common to all membership and H_0 . In physical mass, the same clumps form in 1k and 16k models, almost regardless of the duration of the expansion. We note a mass transfer from small to high mass clumps when H_0 increases, that is consistent with a merging process: small clumps assemble or get accreted by large clumps. When the initial expansion is strong, the merging lasts longer and more mass is transferred. This is confirmed by visual inspection of the models, as we see clumps merging during the expansion.

3.2.2 Influence of stellar mass function

Neither H_0 or N seem to heavily influence the shape of the clump mass function. We now turn to another parameter: the stellar mass function. We know the clumps are seeded by density fluctuations in the initial uniform sphere. These fluctuations are governed by pure Poisson noise in the case of identical stellar masses, but are modified and enhanced once stars follow a mass function themselves: a high-mass star surrounded by lighter ones will by itself introduce a localized strong density fluctuation. We expect a relation between the clump mass function and the *stellar* mass function in the generated initial conditions.

We wish to quantify this relation. To this end, we ran a set of simulations where all the stars have the same mass, and two sets for which a Salpeter mass function with $\alpha = 2.35$ was truncated at different upper- and lower-bounds. A total of 15000 stars in a Hubble configuration were used, all let go with the same initial expansion rate $H_0 = 1$. For the multi-mass models, the mass range was chosen as $[0.3, 100] M_\odot$ and $[0.35, 20] M_\odot$ so that the mean stellar mass $= 1 M_\odot$ as for the single-mass models. Thirty different runs were performed in each case and the outcome averaged for better statistics. These are referred to as Rmh1, Rmh100 and Rmh20 in Table 3.1.

On Fig. 3.8, we display the number of clumps as function of clump mass for the truncated Salpeter models as a red solid line, while the single stellar mass models are shown in green dash. A grey shade indicates one standard deviation where statistics allow (*i.e.*, large numbers), and, as in previous section, we have used bins of constant logarithmic mass intervals. Fig. 3.8a shows Rmh20 models, and 3.8b shows Rmh100 models. With clump membership restricted to $N \geq 12$, the identical-mass model stays relatively close to a power law (straight dotted line on

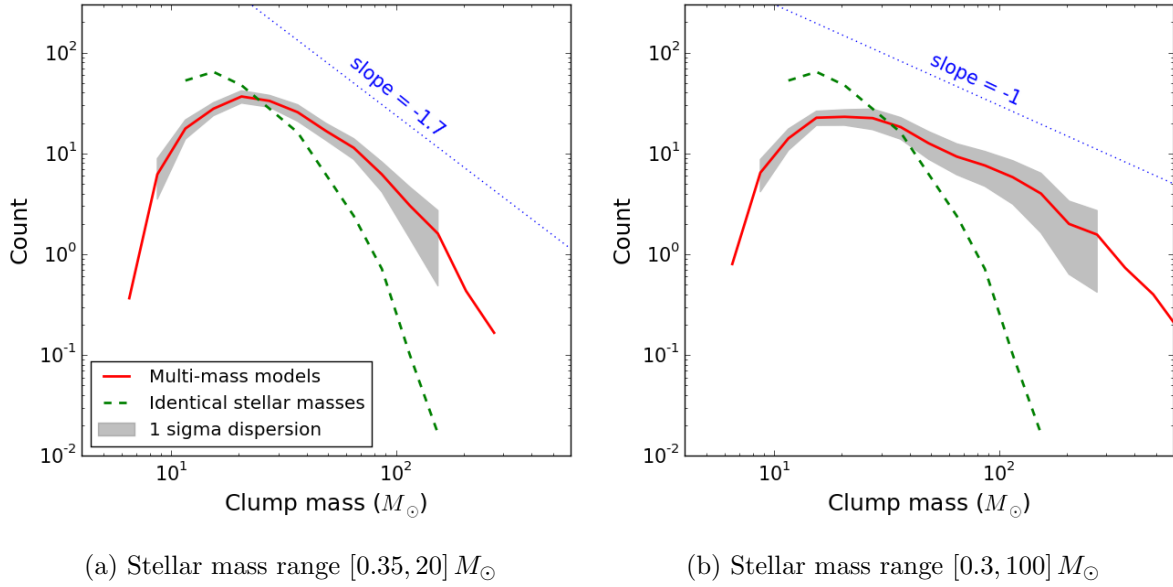


Figure 3.8: Mass function of the clumps identified with the MST algorithm. The calculations all had $N = 15000$ stars, and we have averaged over 30 realisations for each configuration. The results for three stellar mass functions are displayed : a model with equal-mass stars (green dashed line) ; a Salpeter distribution function truncated at $20M_{\odot}$ (solid red line, left) ; a Salpeter distribution function truncated at $100M_{\odot}$ (solid red line, right). (a) The clumps mass function for equal-mass models shows a trend with mass roughly in agreement with an M^{-4} power-law. By comparison, the results for an Salpeter stellar distribution function truncated at $20M_{\odot}$ has a bell-shaped profile, with a peak around $M = 20.5M_{\odot}$; only the tail-end shows marginal agreement with an $\propto M^{-1.7}$ power-law (dotted line on the figure) ; (b) another Salpeter distribution function but with the upper-mass truncation set at $100M_{\odot}$. The tail at large clump mass is now much flatter, with a slope $\approx M^{-1}$, (dotted line on the figure as well). The bins used had constant logarithmic mass intervals.

the figure) of index ≈ -4 for the higher mass clumps. A spread in stellar masses leads to much more massive clumps (we counted $\simeq 80$ clumps of $12M_{\odot}$ for the equal-mass case ; and ≈ 32 with a mass $\leq 12M_{\odot}$ for the other ones) . This transforms the clump mass function, from a near-power-law, to a bell-shaped distribution.

When very massive stars are included in the calculations, yet more massive clumps are formed (Fig. 3.8b). The formation of large sub-structures depletes the number of clumps around the peak value, and so the distribution becomes broader and shallower. The mean clump mass for the different cases read $20M_{\odot}$ (equal-mass), $32M_{\odot}$ (Salpeter $m_{max} = 20M_{\odot}$) and $45M_{\odot}$ (Salpeter $m_{max} = 100M_{\odot}$), a steady increase with the width of the stellar mass spectrum. On the other hand, the position of the peak of the distribution remains unchanged at (roughly) 20 to $21M_{\odot}$. The trend in total number of clumps detected is a slight *decrease* with the broadening of the stellar mass spectrum, from 187, down to 151 respectively for the $m_{max} = 20$ and $100M_{\odot}$ Salpeter models. We observe that the overall fraction of stars found in clumps (some ≈ 6500 out of 15000, or 43%) stays unchanged.

We argue that the shape of the clump mass spectrum provides indirect evidence for the role of massive stars predominantly as seeds for growth in our simulation. This is to be opposed to a full hierarchical build-up of clumps from very tiny sub-structures. There are two tell-tale signs to support this view : a) if high-mass clumps formed through the repeated and stochastic merger of small clumps, then the clump mass function should tend to a log-normal distribution, which is symmetric (in logarithmic scales) with respect to the peak value, whereas the distributions shown here lack this basic property ; and b) the ratio of maximum clump mass to mean mass

may exceed 15 when the stellar truncation mass is set to $20 M_{\odot}$, and reaches only ~ 4 in the case when the upper mass is set to $100 M_{\odot}$. If small-ish clumps were merging at the same rate in both models, then this ratio should be comparable. Instead, very large clumps take too long to assemble and the merger rate drops with clump mass. Recall that all fragmentation calculations ran for the same total time. There is a weak merging process happening, as shown in the previous section, but it is marginal, as heavy clumps likely form from massive star seeds.

To check this hypothesis, we borrow from black hole dynamics in galactic nuclei the notion of a *radius of influence*, which is the radius enclosing as much mass in the stars as the central black hole mass (see e.g. Merritt 2013). Here, the stars inside the influence radius are bound to the massive star at the centre. Thus if a massive star is a seed for a clump, and only the stars inside the influence radius remain bound to it, we should count as many clumps in the mass range $2m_{\star}, 2m_{\star} + 2dm_{\star}$, as there are stars in the range $m_{\star}, m_{\star} + dm_{\star}$. The maximum clump mass exceeds twice that of the most massive stars m_{max} , which implies some degree of merging and is consistent with the previous section. If we count all clumps starting from the truncation value m_{max} of the stellar mass function, then we should find as many clumps in the mass range above m_{max} , as there are stars in the interval $[m_{max}/2, m_{max}]$. We find for runs with $m_{max} = 20 M_{\odot}$ some 120 clumps more massive than that, when there are $\simeq 100$ stars in the range $[10, 20] M_{\odot}$, essentially identical ; and some 14 clumps of $100 M_{\odot}$ or more, when there are (on average) 9 stars in the mass range $[50, 100] M_{\odot}$. This calculation suggests that most massive stars act as seeds for the formation of large clumps in the generated initial conditions.

3.3 Clump contents

In this section we compare the clump configurations derived from the Hubble-Lemaître expansion method with the distribution of proto-stars that form in hydrodynamical simulations. We first look at the velocity field inside and outside the clumps, then we investigate the stellar content of the clumps themselves and their mass segregation.

3.3.1 The velocity field

There is no hydrodynamics in the approach that we have taken, nevertheless expansion under gravity alone is equivalent to the adiabatic expansion of gas : for that case, the first law of thermodynamics equates the drop in internal energy dU to minus the external work, $-pdV$. At constant mass, the change in gravitational energy dW is $-dE_k$, where E_k is the kinetic energy. With $W < 0$ but increasing over time, this implies that E_k drops in amplitude. In the case when the motion is strictly radial, $E_k = 0$ when $H = 0$ and all stars come to rest. We ask to what extent the growth of substructures and non-radial motion off-set the ‘adiabatic cooling’ brought on by expansion.

Fig. 3.9a graphs the x-axis one-dimensional velocity distribution for the R40h100 model. The left-hand panel displays the overall distribution as well as the two sub-populations of clumps members and out-of-clump *field* stars. We identified some 20944 stars in clumps (or $\approx 52\%$) at the end of expansion. The expectation that all stars have zero- or low-velocities is validated by the peak in the distribution around $v_x = 0$.

As sub-structures form and interact mutually, generating tangential as well as radial motion, the peak broadens but remains symmetric about the origin. The large velocities are brought by stars in clumps, which demonstrates that interactions within the substructures boost the internal velocity dispersion of the cluster as a whole. Field stars dominate the low-amplitude regime. Their velocity distribution is well-fitted with a Gaussian (shown as a dotted blue line), down to one-tenth the height of the central peak, or about 1% of all field stars.

To illustrate further the idea that large velocities are confined to clumps formed by fragmentation modes, we compare on Fig. 3.9b a set of models with different initial values of H_0 : 0, 0.3,

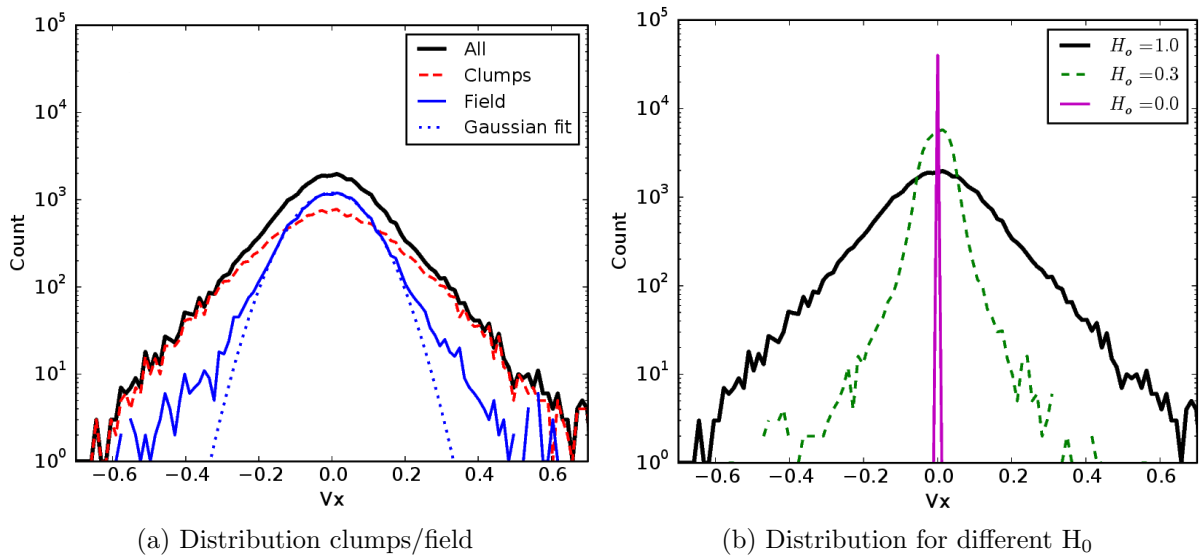


Figure 3.9: (a) Distribution of the one-dimensional velocity field for the whole cluster as the thick solid black line, in the simulation labelled as R40h20 at the apex time ($H = 0$). The red dashed distribution matches clump members and thin solid blue the field particles. (b) The distribution for three different values of H_0 : when $H_0 = 0$, the distribution is a Dirac- δ around $v = 0$. The central distribution broadens as H_0 increases to 0.3 and 1. Observe the exponential profiles at large $|v|$. Velocities are in $H.u$

and 1. Clearly when $H_0 = 0$, the velocities are identically zero and there is no fragmentation whatsoever (apart from root-N noise). The distribution is then a sharp peak centered on zero. For positive but low values of H_0 , the fragmentation modes do not develop much before the apex and the (non-radial) velocities remain small. The central peak has a much narrower dispersion, and the high-velocity wings are clipped. In this case, too, analysis of the weakly fragmented system shows that virtually all high-velocity stars are found in clumps. The velocity distribution for the case $H_0 = 1$ is added for comparison. The fact that the full range in velocities is reduced by a factor ~ 3 for the less fragmented model is also an indication of the shallower potential well of the clumps

The full population velocity distribution (solid black line) at first sight is very similar to those of [Klessen & Burkert \(2000, Fig. 5\)](#). In that figure, the authors show the velocity distribution of gas particles in a fragmenting system. [Klessen & Burkert](#) attribute the high-velocity tails to gas particles falling towards stellar clumps at supersonic speed. Supersonic motions imply that gas particles trace ballistic trajectories, and hence behave like point mass particles.

A small fraction of field stars in our calculations also have large velocities. We suspected that these stars might have acquired their large velocity through in-fall toward a nearby stellar clump. We did not, however, find compelling evidence that would allow us to identify the origin of high velocities in field stars. Inspection of a sequence of snapshots failed to show that the velocity vectors were pointing at nearby stellar clumps: it is therefore not possible to make the same assertion as [Klessen & Burkert](#) and state that stellar clumps accrete some field stars.

It is possible, on the other hand, that high velocities originate from past star-star interactions. However, we did not find clear trends in the few orbits that we studied which would confirm such an event. The question of mass accretion by stellar clumps might be best settled if we added gas to our simulations to boost the mass resolution, and analysed model data using mock CCD frames, as did [Klessen & Burkert](#). This was not attempted here.

We close this section with a remark about the velocity distributions seen on Fig. 3.9 and the internal state of the stellar clumps. Because small clumps would have time to evolve dynamically through star-star collisions and reach a state of near-equilibrium (see §2.2.4) we would expect

clumps to develop a velocity field similar to Mitchie-King models of relaxed self-gravitating star clusters (Binney & Tremaine, 2008). The one-dimensional velocity distribution of Mitchie-King models plotted in a logarithmic scale approaches a flat-top when $|v_{1d}|$ is small, and cuts-off rapidly at large values : the distributions are concave at all velocities. This holds true for all models independently of their King parameter¹ W_0 .

The shape of the distributions displayed on Fig. 3.9, on the other hand, is convex as we shift, from small, to large $|v_{1d}|$. We deduce from this straightforward observation that the clumps that formed through fragmentation and subsequent mergers cannot be treated as fully in isolation and in dynamical equilibrium à la Mitchie-King. Fragmentation in hydrodynamical calculations often proceeds from filaments and knots (e.g., Klessen & Burkert 2001; Mac Low & Klessen 2004; Maschberger et al. 2010; Bate, Tricco & Price 2014). The clumps that form in a fragmenting Hubble flow are also surrounded by filaments and other structures which perturb them.

3.3.2 The stellar mass function in clumps

We show on Fig. 3.10 the mass function of stars both in clumps, field and in the whole cluster. For brevity, we only show a model with a mass function truncated at $20M_\odot$, Rmh20, however our conclusions are not sensitive to the truncation value. The mass function of ≈ 6400 stars that were found in clumps (some 43%) is displayed as the red solid curve and all other stars, field stars, as the blue solid curve. The theoretical Salpeter distribution function for the same number of stars is shown in black dots, with grey shades giving the 1σ dispersion from multiple samplings. Finally, the green dashed curve shows the mass distribution of all 15 000 stars in the model. The lower panel is the same data normalised to the Salpeter data.

The uptake in massive stars for the whole population (green dashed line) of both clumps members and field stars is a statistical artefact and lie within the standard deviation of a Salpeter distribution with comparable sampling number.

The clump member population clearly deviates from a Salpeter distribution in two ways : first we note a deficit of low mass stars with respect to the theoretical Salpeter; secondly, although a Salpeter mass function is more or less consistent with the population up to $M \approx 2M_\odot$ (black dotted line) the distribution shows a clear excess of massive stars. We find that practically all the stars more massive than $10M_\odot$ ended up in a clump (this is the point where the solid red curve joins the dash green one).

A linear regression fit of the clump members mass function gives a power-law index of -2.15 ± 0.02 , shallower than the Salpeter index of -2.35. Applying the same analysis to field stars, we find a steeper mass function of index -2.46 ± 0.02 . The difference of ≈ 0.3 between the two populations is very similar to what is found in the Milky Way disc (see e.g. Czekaj et al. 2014; Rybizki & Just 2015; Bastian, Covey & Meyer 2010)

Bonnell, Vine & Bate (2004) and Maschberger et al. (2010) showed from inspection of hydrodynamical simulations that massive stars play a key role in the assembling process of clumps, attracting already formed protostars to them. We find a similar general trend in Hubble-fragmented gas-free simulations: clumps develop around massive stars so that their stellar mass function is top-heavy.

This excess can also be seen in the top panel of Fig. 3.11a in which for each of 440 clumps, we show as white dots the mass of their heaviest star as a function of the host clump's mass. These data were obtained from the R40h100 run. For comparison, we sampled a Salpeter mass function, drawing the same number of stars as found in each clump. We then identify the most massive star in the Salpeter sample ; the procedure was repeated 15000 times *for each clump* to obtain suitable statistics. The grey shades (color levels in the electronic version) shows the resulting distribution.

In a nutshell, Fig. 3.11a shows for each clump the likelihood that their most massive stars

¹Notice how this holds only because of the choice of a logarithmic vertical axis.

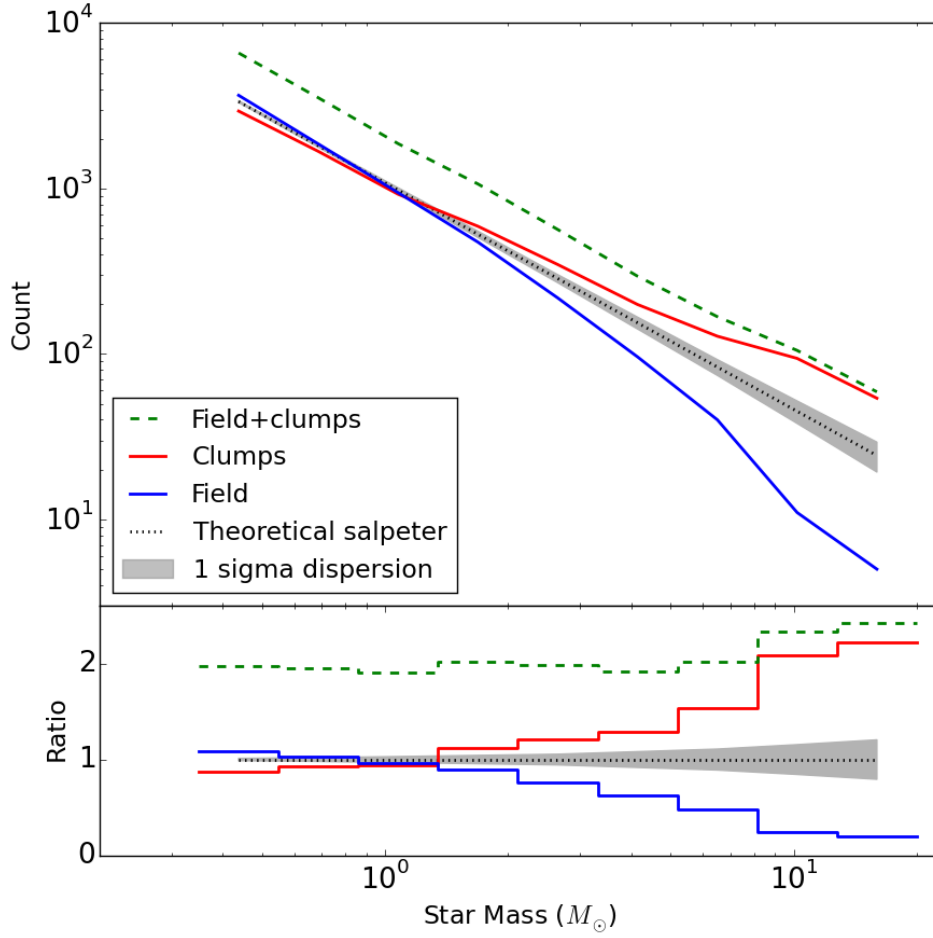
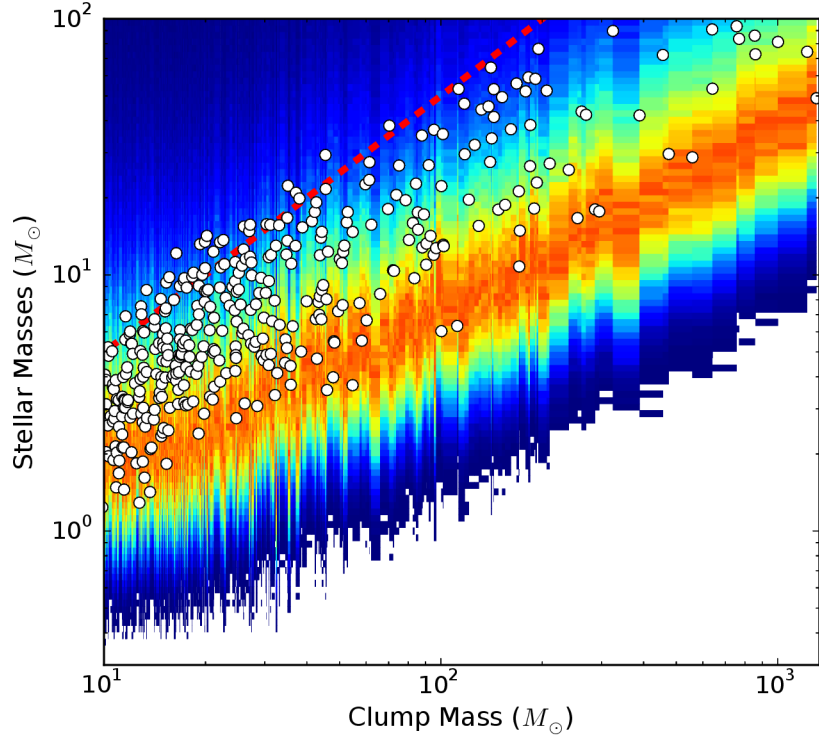
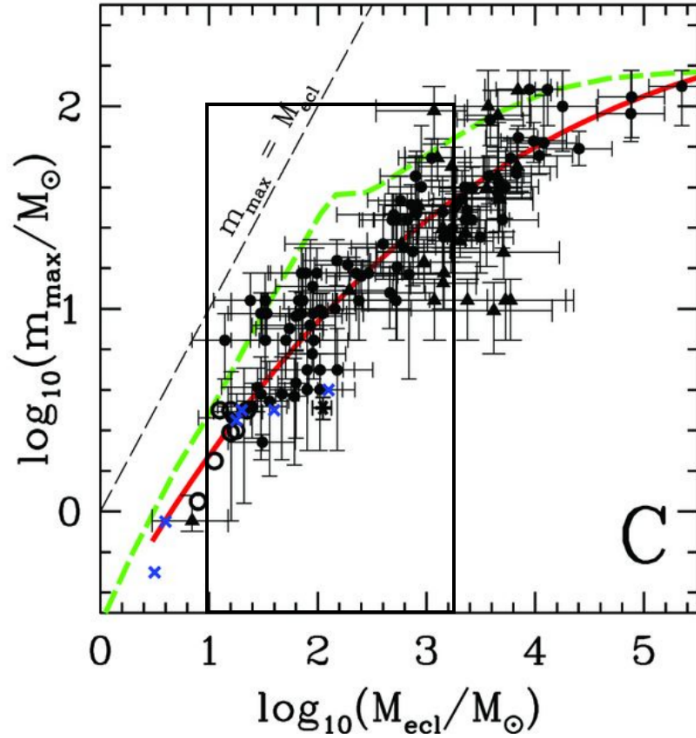


Figure 3.10: Top panel : Mass function of all stars belonging to a detected clump (solid red). The expectation drawn from a Salpeter distribution function for the same total number of stars in dotted black ; the grey shade are 1σ uncertainties. The green dashed line is the distribution for the full cluster. Bottom panel : same data normalised to the Salpeter expectation.



(a) Distribution clumps/field



(b) Distribution for different H_0

Figure 3.11: (a) Mass of the heavier star in each clump, shown as white dots, as a function of clump mass. The color map shows the likelihood for the maximum mass if all clump members were sampled from a Salpeter IMF ; the orange crest gives the maximum likelihood. The red dashed line shows the relation $m_{clump} = 2m_{max}$ (see. section 3.2.2). The data was taken from the R40h100 run. (b) is a similar distribution from Weidner, Kroupa & Pflamm-Altenburg (2013), built with data about young embedded star clusters from Weidner, Kroupa & Bonnell (2010). The black frame notes the range of masses displayed in (a).

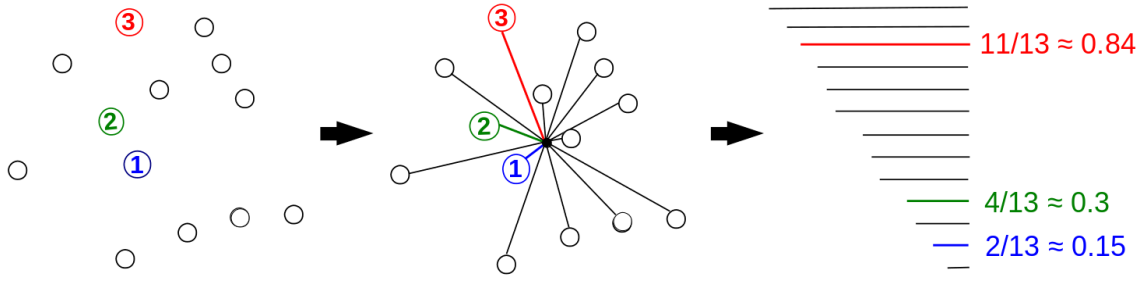


Figure 3.12: Illustration of the radial ranking method. Stars marked 1,2 and 3 are the first, second and third most massive stars in the clump. Distances to the geometrical center are computed then sorted. The position in the sorted list is converted to a number, the radial rank.

may be drawn from a Salpeter function, one could call the red maximum likelihood zone the “Salpeter valley”. Only clumps with a mass $> 10M_{\odot}$ are included to account for a possible bias when clump membership reaches below $N_d = 12$ stars. It can be seen on the figure that the scatter of white dots tends to lie systematically above the Salpeter valley. If we add the relation $m_{clump} = 2 \max\{m_{\star}\}$ (cf. section 3.2.2), we find some overlap with the data (see the red dashed line on Fig. 3.11a). This clearly illustrates the tendency for massive stars to act as seeds when the clump form, while the scatter is driven by the merger and accretion history of individual clumps.

The correlation displayed on Fig. 3.11a is in good agreement with observational data for young embedded clusters of the same mass range published by Weidner, Kroupa & Pflamm-Altenburg 2013. We reproduced their figure on Fig. 3.11b with a black frame representing the range shown on Fig. 3.11a.

Note how the *scatter* in the correlation brought on by the dynamical processes at play during the adiabatic fragmentation phase also compares well with the data. Thus the stellar clumps modelled here recover an important characteristic of observed embedded young clusters.

3.3.3 Mass segregation

In this section, we ask whether the clump assembling process at play in our simulations accounts for the mass segregation measured in star-forming cores in hydrodynamical simulations. The measure of mass segregation of Olczak, Spurzem & Henning (2011) based on the MST, while efficient, will give noisy results for very small-N clumps. Instead, we follow Maschberger et al. (2010) and rank clump members according to their distance to the geometric centre of a clump, which is calculated by number-averaging (so this centre is not the clump barycentre). We then sort the bodies by mass and tabulate the radial rank of the three most massive ones. This process is illustrated on Fig 3.12.

The great advantage of this approach is that it is independent of geometry and absolute size once the ranking is normalised to the clump membership N_c . One issue arises with the binning of the rank, since small values of N_c give large intervals by construction, and conversely for populous clumps : we found a good compromise by setting the width of each bin to $1/20$ since the mean clump mass $\sim 20M_{\odot}$ implies $N_c \sim 20$ on average. The procedure is repeated over all clumps identified in the run (typically on the order of ~ 200). The diagnostic for an un-biased sampling is a profile with radius that remains the same regardless of the mass selected ; if, furthermore, the stars are (on the mean) un-segregated in radius, then the profiles will be flat.

Fig. 3.13 graphs the distribution of rank of the three most massive stars in all the clumps from R40h100 fragmented state. The salient features are that 1) none of the distributions are

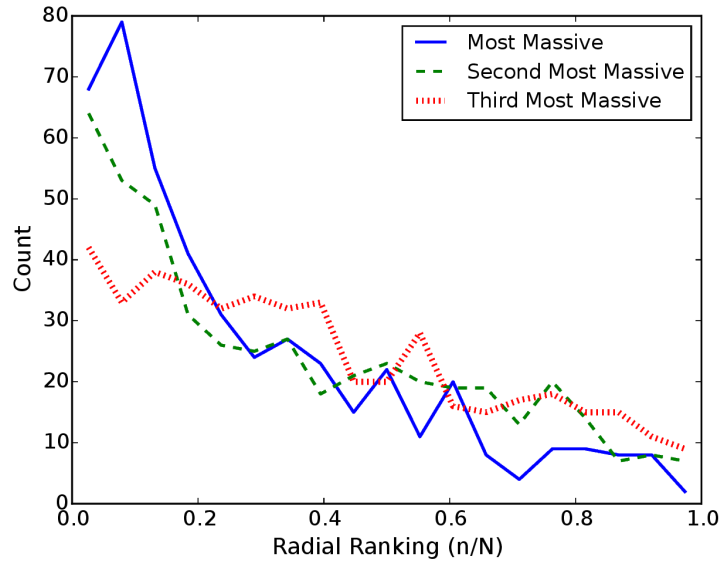


Figure 3.13: Histograms of radial ranking of first, second and third most massive star in each clump for a model with $N = 40\,000$ stars (R40h100).

flat, all three peaking significantly at small ranks ; and 2) there is a clear trend for the most massive star also to be the most segregated. Precisely this result had to be expected from the internal dynamics of small clumps (cf. section 2.2.4). Our Fig. 3.13 should be compared with Fig. 13 of Maschberger et al. (2010): the authors also found radial rank distribution to peak at small values for massive stars, showing a level of mass-segregation in their clumps.

It is striking that the measure of mass segregation attained here for a gas-free configuration is a good match to a full hydrodynamical setup. By implication the segregation proceeds more vigorously once the proto-stellar cores have condensed and behave essentially like point sources. The initial configuration that we have adopted relies only on density fluctuations to seed clumps, however once again we find evidence that massive stars begin and remain the centre of gravitational focus for clump formation. That is not so when clumps are setup using a fractal approach (Goodwin & Whitworth, 2004; Allison et al., 2009a). There is then no segregation initially, and it all develops at or shortly prior to the global system evolution towards equilibrium (the collapsing violent relaxation phase).

3.4 Concluding remarks

We have developed a new approach based on adiabatic fragmentation to set up self-consistent configurations for stellar dynamics that link up the velocity field of stars to their irregular space configuration of arbitrary geometry, such as knots or filaments. The method offers great advantages: it is easy to implement; it can treat an arbitrary number of stars without any resolution issue; furthermore, the level of fragmentation can be tuned through the Hubble parameter. The light computational load allows for statistical ensemble averaging over large samples, as was done throughout this chapter. For instance, the computation time on a single card for 80,000 stars is about 12 hours. The methods has its limitations: the most significant one is the failure to include hydrodynamical effects. In the introduction, we mentioned other approaches partly based on hydrodynamics: such hybrid methods have been successful but remain limited in scope, for instance Moeckel et al. (2012), or demanding in computational resources (and so constrain the number of realizations), as in Fujii & Portegies Zwart (2016).

The importance of massive stars

During the fragmentation process in our models, heavy stars act as seeds for the growth of stellar clumps, and so the stellar clumps mass spectrum is shaped by the mass function of the available *stars*. Although the fragmentation through gravitation only does not include the detailed physics of star formation, we noted that hydrodynamical calculations including gas pressure and turbulence suggest that the gravitational potential of massive stars attract more gas and stars and, as such, act as seeds for the formation of clumps (Bonnell, Vine & Bate, 2004). We therefore recover a key prediction of hydrodynamical simulations. It is then interesting to ask whether observations show a correlation between the host clump mass and its population of massive stars.

Based on analysis of our fragmented Hubble models, we recover on Fig 3.11 a correlation between the maximum mass of a star found in a clump of a given mass, M_c . This $\max\{m_\star\} - M_c$ relation is eerily similar to the compilation for young clusters by Weidner, Kroupa & Pflamm-Altenburg (2013), from which we extracted the figure 3.11b. Furthermore, we also found that the stellar mass function in clumps has a much flatter (top-heavy) profile than in the field, *i.e.* stars that do not belong to any clump: power-law fits for the two stellar populations show that the Salpeter index for clumps stars is lower by about ≈ 0.3 compared to the same index for field stars. A similar difference is deduced for Milky Way data (Czekaj et al. 2014; Rybizki & Just 2015; see also Fig 2 from Bastian, Covey & Meyer 2010): we argue that these characteristics will help tighten our understanding of the long-term evolution of such stellar associations, given that their properties are, on the out-set, close to actual data for young clusters. It should be emphasised that the global index of external galaxies may differ significantly from the canonical value $\alpha = 2.35$ (*e.g.*, the GAMA survey, Gunawardhana et al. 2011; see also Hoversten & Glazebrook 2008). We have not explored here to what extent this difference in indices between field and clump populations will change for other values of the global index α .

We have also noted that the clumps are *mass segregated* at birth, *i.e.* at the end of the fragmentation process. When we apply the same ranking statistics as for hydrodynamical calculations of star formation, we obtain the same level of segregation for the three most massive stars in a clump (cf. Fig. 3.13).

The slope of the clump mass function

Klessen & Burkert (2000, 2001) fit the gas clump mass function of their simulations with a power-law of index $-3/2$. On the other hand, the *cluster* mass function in the Milky Way can be described as a power law $\frac{dN}{dM} \propto M^{-\beta}$ where β takes value ranging from -2 to -2.4 (Haas & Anders, 2010). We have indicated that a power-law relation with a slope $\beta \simeq -4$ is a rough fit for the case where all the stars are identical (Fig. 3.8). This is not so when a stellar mass spectrum is included : if a Salpeter distribution function is truncated at $20M_\odot$ a power-law with slope $\beta \simeq -1.7$ still fits approximately the distribution of clumps of mass $> 20 M_\odot$; and when the Salpeter distribution function is truncated at $100M_\odot$, a power-law similarly fits the tail-end of the distribution but now with a slope of $\simeq -1$ (see Fig. 3.8b). It is intriguing that the slope of the distribution should fall within the bracket of values for the observational data for clusters (-2.4^+) and hydrodynamical fragmentation models ($-3/2$). If the clumps formed from hydrodynamical fragmentation should become individual star clusters, and recover the $\beta \simeq -2$ or lower slope of observational data, then the distribution function must become steeper and also cover a broader range of masses. The same conclusion applies to the Hubble clump distribution function.

This implies either that clumps will merge so that a few very massive clusters will emerge, or that fewer massive clumps form in the first place. Comparison with existing cluster population needs us to assume these clumps do not fall back and merge through collapse. This is possible with an adequate galactic tidal field ripping apart this fragmented configuration and isolating the

clumps before the collapse. Many of the small stellar overdensities detected as clumps would not survive more than a few million years before dispersing through dynamical interaction, however the larger clumps could survive and appear as isolated cluster or part of an association. These massive clumps are the key to comparison to the galactic cluster mass function. We have shown how the stellar IMF provides seeds for the growth of massive clumps and have illustrated this with a Salpeter power-law IMF. A more realistic IMF has a steeper power index at larger stellar masses ([Kroupa, 2002](#); [Chabrier, 2005](#)). The fragmentation of stellar systems with fewer massive stars would deplete the clump mass function at larger masses more in line with observed statistics for clusters. This variability in the clump mass function highlights the major influence of the stellar IMF on the fragmentation process. A full exploration of fragmentation requires hydrodynamical simulations, which we have not performed here. These simulations remain limited to much smaller systems ([Bate, Tricco & Price, 2014](#); [Lomax et al., 2014](#)).

In the next chapter we assume an absence of tidal field and follow through with the final stage of evolution towards equilibrium. We compare the final configuration with those of [Allison et al. \(2009a\)](#) and the recent study by [Caputo, de Vries & Portegies Zwart \(2014\)](#).

CHAPTER 4

Collapse and dynamical evolution

In this chapter, we let the Hubble-Lemaître models evolve and undergo violent relaxation. We compare their dynamical evolution with that of cold uniform models. We investigate the evolution of the structure and global mass segregation.

Contents

4.1	The simulations	65
4.1.1	Description of the models	65
4.1.2	Scaling to physical units	66
4.1.3	Removal of the ejected stars	67
4.2	Collapse and virialisation	68
4.3	Global mass segregation	72
4.4	Concluding remarks	75

4.1 The simulations

4.1.1 Description of the models

The Hubble-Lemaître fragmented system is subvirial by construction. The configuration we took as a reference is the apex of the expansion: the kinetic energy initially injected in the expansion has been converted into potential energy through expansion or converted to transversal motion by two-body interaction. If the model is left to evolve further, it collapses, violently relaxing to reach a quasi-equilibrium state, resembling a Plummer or King model.

In the present chapter, simulations will use the fully fragmented state of Hubble models as initial conditions for the subsequent dynamical evolution. Observational clues point to collapsing and violently relaxing clusters. For example, [Cottaar et al. \(2015\)](#) find IC348, a young (2-6 Myr) cluster, to be both survirial and with a convergent velocity field, consistent with infalling motion. Our models undergo dry collapse with no gas, while real objects such as IC348 still contain residual gas. The scenario of our simulations is an idealized situation: clearly if there was residual gas between the clumps and it was evacuated through stellar feedback, both the clump merger rate and the depth of the potential achieved during relaxation would be affected. As a limiting case, rapid gas removal may lead to total dissolution (see for instance [Moeckel et al. 2012](#) and [Fujii & Portegies Zwart 2016](#)). In the current situation, all clumps will merge.

The numerical integration were done once more with the Nbody6 integrator with the same computational units. For comparison purposes, we also performed simulations of cold uniform sphere, a configuration which has been extensively used in the past (e.g., [Theis & Spurzem 1999](#); [Boily, Athanassoula & Kroupa 2002](#); [Barnes, Lanzel & Williams 2009](#); [Caputo, de Vries & Portegies Zwart 2014](#); [Benhaiem & Sylos Labini 2015](#)) and one that minimises the level of

fragmentation and mass segregation in the on-set of collapse. The models are referenced as Rh100, Rh20, Ru100 and Ru20 in Table 3.1. We focus here on models with a mass function from $0.35M_{\odot}$ to $20M_{\odot}$ and 15000 stars, a compromise value for rich open clusters that should allow us to identify clearly collisional effects and trends with time, and ease comparison with the recent study by [Caputo, de Vries & Portegies Zwart \(2014\)](#) where most calculations are performed with that sampling. We let both Hubble-fragmented- and uniform sphere evolve up to 40 H.u.

4.1.2 Scaling to physical units

Before discussing the results, it is useful to translate the units of computation to physical scales. This is important if we want to discuss the state of the systems using one and the same physical time, such that the hypothesis of no stellar evolution holds good. To do so, we compute the free-fall time of an uniform sphere (a good approximation for fragmented model as well) both in physical units and Hénon units, which provide a conversion factor. We first have to choose an initial physical length scale for the system by setting $R_h = 1$ pc. With a total system mass of $M = 15 \times 10^3 M_{\odot}$, this gives a half-mass volume density

$$\rho_h = \frac{M/2}{\frac{4}{3}\pi r_h^3} \simeq 1.8 \times 10^3 M_{\odot}/pc^3, \quad (4.1)$$

well within values typically inferred from observations.

The free-fall time of an uniform sphere, obtained from conservation of energy and integration, is expressed:

$$t_{ff} = \sqrt{\frac{3\pi}{32G\rho_h}} \quad (4.2)$$

Computing $\rho_{h,\text{Hénon}} \simeq 0.13$, we can now compute both values of the free-fall time:

$$t_{ff} \simeq 1.5 t_{\text{Hénon}} \quad (4.3)$$

$$\simeq 0.2 \text{ Myr} \quad (4.4)$$

Which gives:

$$1 t_{\text{Hénon}} \equiv 0.13 \text{ Myr} = 1.3 \times 10^5 \text{ yr} \quad (4.5)$$

Thus by running up to 40 H.u we ensure that the systems evolve for $\sim 6\text{Myr}$ years, about the lifetime of a $50M_{\odot}$ star. ¹

We now want to evaluate the crossing and relaxation timescales in such a system, as they were defined in the introduction (1.2.2), and how they relate to the total duration of the simulation. We could attempt to derive a crossing time for the initial, subvirial state but it would not be representative of the evolution of the system. Instead, the more useful crossing time has to be computed from the equilibrium state achieved. Using the virial theorem and conservation of energy, we can derive dynamical timescales for the equilibrium system. From the definition, the crossing times is defined:

$$t_{cr,eq} = \frac{2R_{h,eq}}{\sigma_{1d,eq}} \quad (4.6)$$

From here on, we write the subscript 0 for initial values and no subscript for equilibrium values. To obtain both R_h and σ_{1d} we start from the total energy of the system. At $t=0$, velocities are null, all energy is potential energy. It can be computed by integrating from the center to R_0 . We obtain

$$E_0 = -\frac{3}{5} \frac{GM^2}{R_0}. \quad (4.7)$$

¹For our models with more massive stars, up to $100M_{\odot}$, these represent only $\sim 5\%$ of the total mass and their removal would not significantly alter the dynamics of the system.

From virial theorem and conservation of energy, we get the following equations at equilibrium

$$\begin{cases} 2E_k + E_p &= 0 \\ E_k + E_p &= E_0 \end{cases} \implies \begin{cases} E_k &= -E_0 = \frac{3}{5} \frac{GM^2}{R_0} \\ E_p &= 2E_0 = -\frac{6}{5} \frac{GM^2}{R_0} \end{cases} \quad (4.8)$$

which can be combined with

$$E_k = \frac{1}{2} M \sigma_{3d}^2 = \frac{1}{2} M (3\sigma_{1d})^2 = \frac{9}{2} M \sigma_{1d}^2 \quad (4.9)$$

to get

$$\sigma_{1d} = \sqrt{\frac{2GM}{15R_0}}. \quad (4.10)$$

As for the half-mass radius at equilibrium, its value is dependant on how concentrated the system is and is not easy to derive. Instead, we replace in Eq. (4.6) the half-mass radius by the virial radius R_v , defined as:

$$E_p = -\frac{GM^2}{2R_v} \quad (4.11)$$

which value should not depart significantly from the half-mass radius and provides an useful approximation. Combining Eq. (4.8) and Eq. (4.11) it comes

$$R_v = \frac{5}{12} R_0. \quad (4.12)$$

Knowing that $R_0 = 2^{1/3} R_{h,0}$, we can now write a good approximation of the crossing time in the relaxed, equilibrium system

$$t_{cr} \simeq 2.28 \frac{R_0^{3/2}}{\sqrt{GM}} \quad (4.13)$$

$$\simeq 3.21 t_{\text{Hénon}} \quad (4.14)$$

$$\simeq 0.5 \text{ Myr} \quad (4.15)$$

With $N = 15000$ we find from (1.6) a two-body relaxation timescale

$$t_{rel} \simeq 380 t_{\text{Hénon}} \quad (4.16)$$

$$\simeq 60 \text{ Myr} \quad (4.17)$$

and from (1.10), considering a mass range of $m_{max}/\langle m \rangle = 20$, we find a mass-segregation timescale

$$t_{ms} \simeq 20 t_{\text{Hénon}} \quad (4.18)$$

$$\simeq 2.8 \text{ Myr} \quad (4.19)$$

Our simulations last for far less than a relaxation time, but we can expect to see some mass segregation set in in our models.

4.1.3 Removal of the ejected stars

The previous section considered there was no mass loss during the collapse and relaxation that leads to the equilibrium system. However, a look at the simulations shows this assumption does not hold. Some stars are ejected from the system after the collapse, when the system bounces.

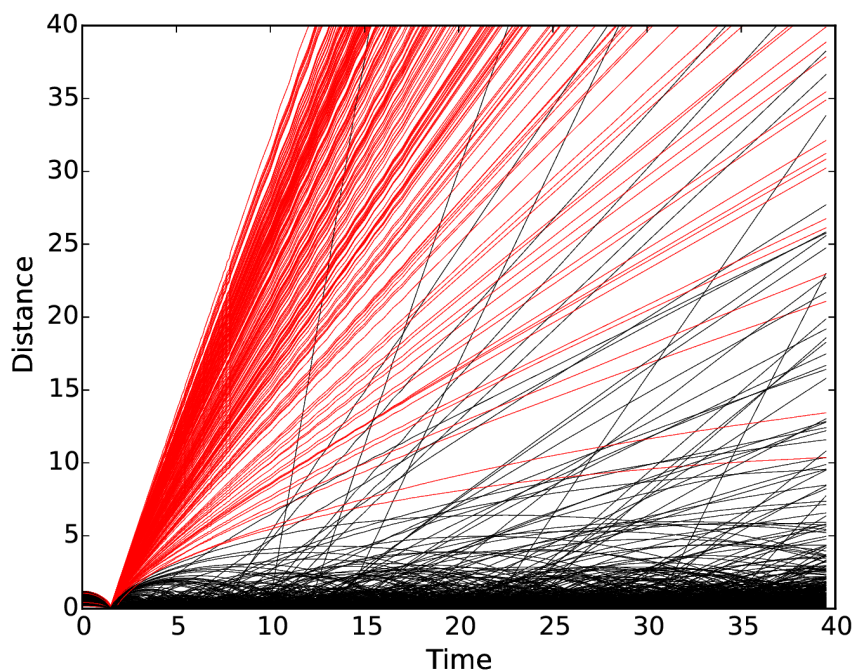


Figure 4.1: Distance to origin for 750 stars from run Ru20 (see Table 3.1). Red lines show the trajectory of stars that are considered ejected according to our criterion.

These stars are not part of the equilibrium system as they have no influence on the central dynamics.

To better understand the evolution of the central, bound system only, we need to isolate and subtract the ejected stars. The obvious way to do this would be to compute the stars mechanical energy and to remove all stars with positive energy. Though this works for a majority of the ejected stars, a subset of them has a marginally negative energy. These register as bound when they are essentially out of the system (far beyond the original system radius).

To collect a maximum number of ejected stars efficiently, we spotted the time when the potential energy is maximum, when the collapse occurs. We then identified all stars whose distance to the center increased monotonically from there onwards. The full selection criteria is therefore :

$$v_r(t) > 0, \forall t > t_{ff} \quad \text{or} \quad E_{\star} > 0, \forall t > t_{ff} \quad (4.20)$$

This allows a more complete selection of the ejecta. On Fig. 4.1 we graph $|\mathbf{r}|$ as a function of time for a subset of escapers (shown as red curves) for the uniform collapse model Ru20. The black curves are trajectories for bound stars given for comparison. Some of these bound stars are later ejected from the system due to two-body interactions, as seen on the figure.

4.2 Collapse and virialisation

The constant diffusion of kinetic energy by two-body interaction means that no stellar system ever reaches a steady equilibrium. However we can contrast the time-evolution of two configurations and draw conclusions about their observable properties.

With this in mind we turn to Fig. 4.2 in which we show the evolution of the half-mass radius for the cold uniform model (labeled Ru20 ; thick red curve), and the Hubble model (labeled Rh20 ; thin blue curve). Both systems have the same bounding radius initially, contract to a small radius when $t \simeq 1.4$ units and then rebound at time $t \simeq 2$ units. When all the stars are

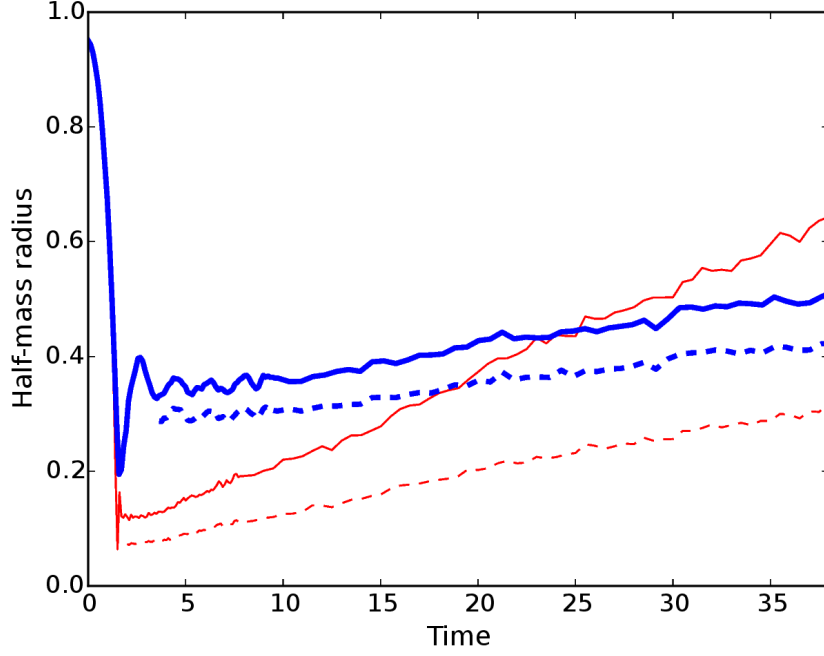


Figure 4.2: Half-mass radius as function of time for two systems undergoing collapse : a uniform-density sphere (thin red solid curve) and a clumpy Hubble model (thick blue solid curve). Half-mass radii are in H.u, as well as the time axis, where $t_{Henon} = 1\text{unit} = 0.13\text{Myr}$. Dashed lines are the half-mass radii of the same systems for the same systems but including only the bound stars.

Table 4.1: Number of initially ejected stars in two collapse calculations

Run	Ejected stars	Ejected mass
Ru20	4227	27%
Rh20	1932	12%

included in the calculation for r_h , we find that the radius increases at near-constant speed after the collapse. That trend does not appear to be slowing down which indicates that a fraction of the stars are escaping. The first batch of escapers is driven by the violent relaxation, however the trend continues beyond $t = 20$ units, corresponding to $t > t_{ms}$ which implies two-body scattering and effective energy exchange between the stars. Note how the uniform model has a much deeper collapse and rebounds much more violently, shedding a fraction twice as large of its stars (Table 4.1). The half-mass radius R_h increases steadily in both models, from the bounce at $t \approx 2$, until the end of the simulation (values in H.u):

$$\begin{array}{llll} R_h \text{ Uniform} & 0.11 & \rightarrow & 0.63 \quad (\times 5); \\ R_h \text{ Hubble} & 0.34 & \rightarrow & 0.49 \quad (\times 1.4). \end{array}$$

Clearly the gentler collapse of the fragmented model has led to a more extended post-collapse configuration and reduced two-body evolution. Observe how the uniform model Ru20 is ejecting more stars than the Hubble model : if we repeat the calculation for the Hubble run Rh20 but now include only the bound stars, the curve of R_h obtained and shown as dash is shifted down but keeps essentially the same slope ≈ 0.004 . By contrast, the calculation for the bound stars of run Ru20 yields a much shallower slope than for the whole system: the slope drops from 0.015 to about 0.007. Irrespective of how the half-mass radius is calculated, the conclusion remains the same and agrees overall with the remark by [Caputo, de Vries & Portegies Zwart \(2014\)](#) that boosting the kinetic energy of the collapsing initial configuration softens the collapse ; this was shown in a different context by [Theis & Spurzem \(1999\)](#) and confirms these older findings. Here, the fragmented model has finite kinetic energy due to the clumps' internal motion. The important new feature brought by the fragmented initial conditions is that the *mass profile* of the virialised configuration evolves much less over time in comparison.

At the bounce, the half-mass radius of the Hubble model is ≈ 4 times larger than that of the of the initially uniform sphere at rest (Fig. 4.2). The half-mass radii overlap at time $t \approx 15 H.u.$ (solid curves) or $t \approx 50 H.u.$ (dashed curves). Is the same trend applicable to all Lagrangian radii? To answer this question we plot on Fig. 4.3 the ten-percentile mass radii for the two models. The results are displayed for the two situations including all the stars (top row) or bound stars only (middle row).

It is striking that the curves show very little evolution at all mass fractions for the case of the Hubble model (see right-hand panels on the figure), whereas all mass shells either contract or expand in time for the uniform one. We have noted how this model should undergo two-body relaxation on a timescale of $t \approx 380 H.u$ while the innermost 10% mass shell shows an indication of *core-collapse* at $t \simeq 5 H.u.$. This is due to the presence of a mass spectrum, the time-scale for core-collapse should be closer to the mass-segregation timescale, $t \simeq 20 H.u.$. The remaining difference can be attributed to the smaller total mass (due to the ejecta) and the various assumptions made in section 4.1.2.

We note here that the two sets of curves reach very similar values at the end of the calculations ($t = 40 H.u$). A key difference between the two models, therefore, is that the final configuration of the Hubble model is almost identical to what it was at the bounce ; the same simply does not hold in the case of a uniform-density collapse. Furthermore, the Hubble calculation shows no hint of two-body relaxation or core-collapse.

[Caputo, de Vries & Portegies Zwart \(2014\)](#) and [Theis & Spurzem \(1999\)](#) noted how a finite amount of kinetic energy in the *initial* configuration alters the depth of the bounce during collapse. The ratio of half-mass radius at the bounce, to its initial value, is then

$$\frac{R_h}{R_{h,0}} \simeq Q_0 + N^{-1/3} \quad (4.21)$$

where Q_0 is the virial ratio of the initial configuration (see [Caputo, de Vries & Portegies Zwart, 2014](#), Fig.5). We computed the kinetic energy of the Hubble configuration and found that the

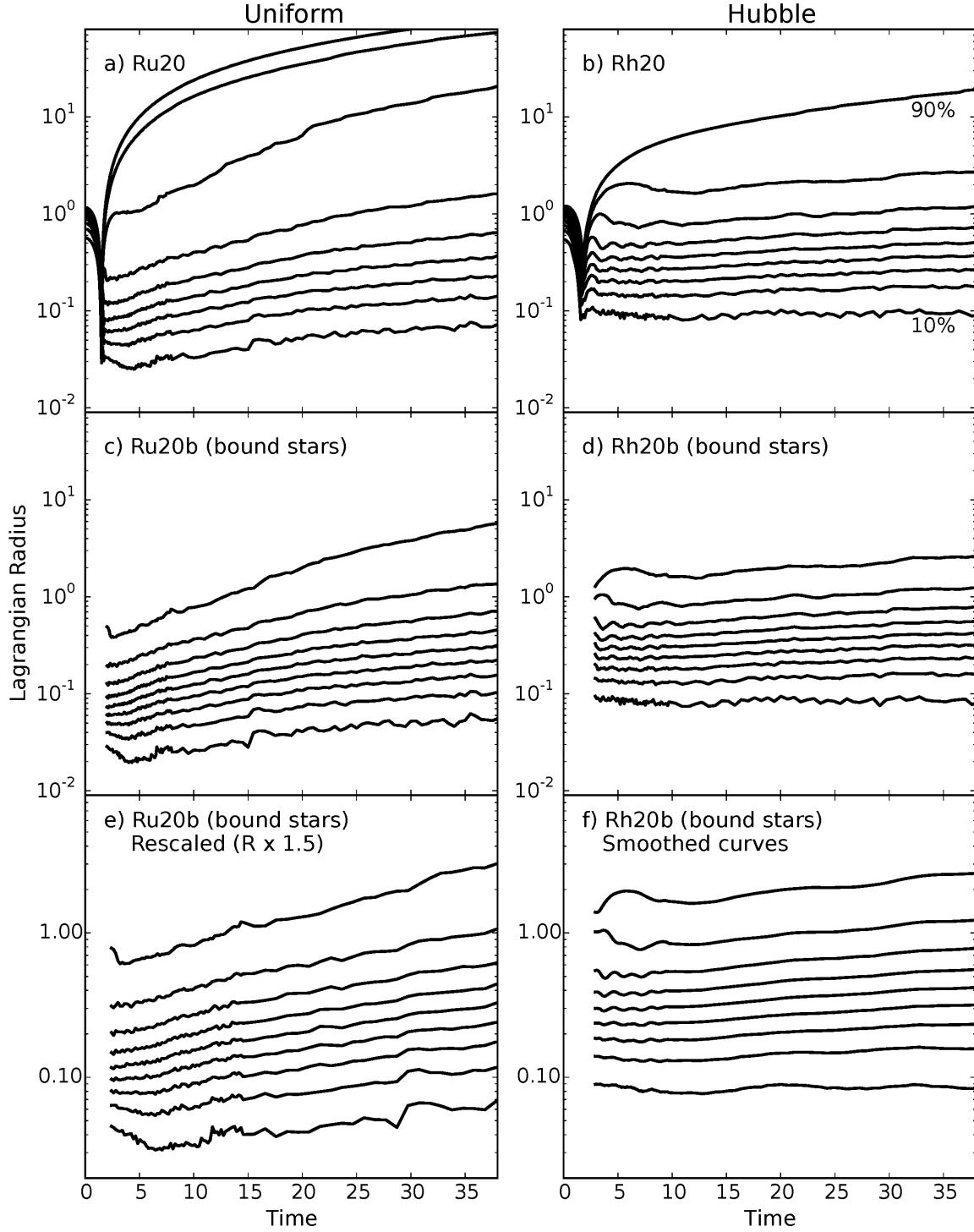


Figure 4.3: The ten-percentile mass radii (10% to 90%) as function of time. Radii and time axis are in H.u, with $t_{\text{Hénon}} = 1\text{unit} = 0.13\text{Myr}$. Left panels show the Uniform model and right panels show the Hubble fragmented models. Panels a and b show the evolution of the whole systems, while panels c and d shows the same radii computed for the bound stars only. Panel e shows the Uniform bound model (Ru20b) for which radius and time were rescaled to compensate the difference of initial kinetic energy (see text for details). Panel f shows the same information as panel d with smoothed data. 10% and 90% radii are labelled in the top right panel.

internal motion of the clumps means that $Q_0(\text{Hubble}) \simeq 0.02$ for a Salpeter mass function with upper truncation value of $20M_\odot$. With $N = 15k$ stars, the ratio $R_h/R_{h,0} \simeq 0.041$ when $Q_0 = 0$ shifts to $R_h/R_{h,0} \simeq 0.061$ when $Q_0 = 0.02$, or a factor close to $3/2$. To account for the difference in kinetic energy of the initial configurations, we may therefore rescale the uniform model such that positions are $\times 3/2$ and the time unit is $\times (3/2)^{3/2} \simeq 1.84$.

The new configuration would evolve in time in exactly the same way after mapping positions and time to their rescaled values. The result is shown as the bottom row on Fig. 4.3. Note that we have blown up the vertical axis to ease comparison between uniform and Hubble models with bound stars only included. The rescaled uniform model is now slightly more extended than before, but overall the final two configurations (at $t = 40 \text{ H.u.}$) are as close as before rescaling. This demonstrates that the outcome of the uniform collapse and its comparison with the Hubble model is not sensitive to a small amount of initial kinetic energy. We note that while the ratio Q_0 is a free parameter in many setups for collapse calculations, that parameter is fixed internally in the Hubble approach.

4.3 Global mass segregation

To investigate the state of mass segregation in our models, we follow the analysis of Caputo, de Vries & Portegies Zwart (2014). The masses are sorted by decreasing values, then subdivided into ten equal-mass bins. This means that the first bin contains the most massive stars. The number of stars in each bin increases as we shift to the following bins, since their mean mass decreases, and so on until we have binned all the stars. The half-mass radius R_h computed for each bin is then plotted as function of time. In this way the mass segregation unfolds over time: if the stars were not segregated by mass, all radii R_h would overlap. If two sub-populations share the same spatial distribution, their respective R_h will overlap.

Figure 4.4 graphs the results for initially uniform-density- and fragmented Hubble models. The layout of the figure is the same as for Fig. 4.3. The violent relaxation phase leads to mass loss for both models and the much more rapid expansion of the half-mass radii of low-mass stars is an indication that most escapers have a lower value of mass.

Fig. 4.4(c) and (d) graphs R_h for the bound stars of each sub-population. Clearly the initially uniform-density model is more compact early on, but note how the heavy stars sink rapidly to the centre, more so than for the case of the Hubble model. The spread of half-mass radii increases with time for both models, however two-body relaxation in the uniform-collapse calculation is much stronger, so that by the end of the simulations the half-mass radii of the low-mass stars of the respective models are essentially identical.

Since the low-mass stars carry the bulk of the mass, that means that the two models achieve the same or similar mean surface density by the end of the run. At that time, the heavy stars in the uniform-collapse calculation are clearly more concentrated than in the Hubble run (compare the radii out to $\sim 40\%$ most massive stars). A direct consequence of this is that the *color* gradients of the core region of a cluster are much reduced when the assembly history proceeds hierarchically, in comparison with the monolithic collapse. It will be interesting and possibly important in future to compare such models with actual data for young clusters.

Another interesting remark is that the kinematics of the stars within the *system* half-mass radius is much different between the two models. For the Hubble calculation, the system half-mass radius, $\approx 0.43 \text{ H.u.}$, at $t = 40$ (cf. Fig. 4.4d) coincides with the half-mass radius of the 30 – 40% bin stellar sub-population. All bins up to that range show little or no time-evolution, around the end of the run, which we interpret as efficient retention of these stars by the relaxed cluster. In the case of the uniform-collapse run, the system half-mass radius reaches $\approx 0.33 \text{ H.u.}$, which is significantly larger than the radius for the 30 – 40% stellar sub-population. For that model, only the bins 0 – 10% and 10 – 20% are flat, and all the others increase almost linearly with time. Thus a fair fraction of bright stars deep in the cluster show systematic *outward*

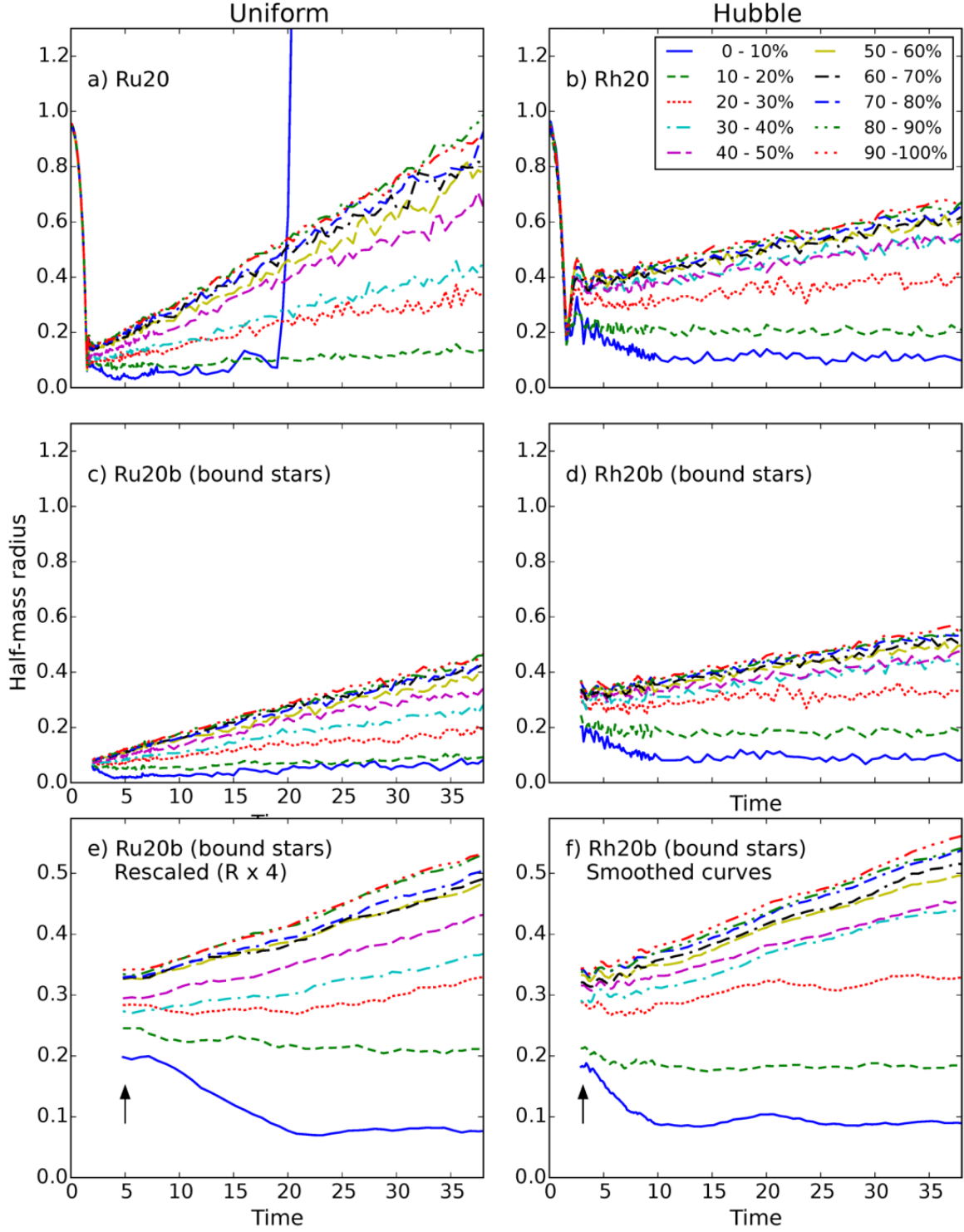


Figure 4.4: Half-mass radii of stars selected by mass as function of time. Each bin identified with 0-10%, 10-20% .. 90-100%, contains ten percent of the total system mass. The stars were sorted by mass in decreasing order, and used to fill each ten-percent mass bin in order. Hence the first ten-percentile contains the most massive stars, the next ten-percentile the second group of massive stars, and so on until the 90-percent bin which contains the least massive stars in the model and is the most populated. Half-mass radius and time are in H.u, with $t_{Henon} = 1 \text{ unit} = 0.13 \text{ Myr}$. Left panels show the evolution of the Uniform model (Ru20, Ru20b) and right panels do the same for the Hubble model (Rh20, Rh20b). The organization of panels follows the same layout than figure 4.3 with a different factor for the rescaling of the uniform system.

Table 4.2: Values of half-mass radii and their ratio to that of the most massive stars. The mass categories are labelled X%-X+10%, with the percent symbol omitted for brevity. The results are for the rescaled bound uniform model (rescaled Ru20b) and the bound Hubble model (Rh20b), after the collapse, and before dynamical mass segregation sets in.

Uniform (%)	0-10	10-20	20-30	30-40	40-50	50-60	60-70	70-80	80-90	90-100
Radius	0.20	0.245	0.282	0.273	0.294	0.325	0.326	0.328	0.335	0.340
Ratio	1	1.23	1.41	1.37	1.47	1.63	1.63	1.64	1.68	1.70
Hubble (%)	0-10	10-20	20-30	30-40	40-50	50-60	60-70	70-80	80-90	90-100
Radius	0.18	0.21	0.286	0.293	0.316	0.321	0.333	0.338	0.342	0.344
Ratio	1	1.16	1.58	1.63	1.76	1.78	1.85	1.88	1.90	1.91

streaming motion, along with low-mass ones. This brings up the possibility to measure this signature motion through relatively bright stars, originating well inside the cluster half-mass radius. Recall that only post-bounce bound stars were selected to compute R_h on Fig. 4.4(c) and (d); the expansion is therefore not driven by chance events (e.g., Fig. 4.4a), but rather through two-body relaxation. On the down side the bright tracers would be short-lived, and this may prove a strong constraint for observational detection.

Given the early dynamical evolution associated with substructured stellar clusters, some observed dense objects may yet be out of equilibrium. We wish to investigate the out-of-equilibrium state of our models just after the collapse. To ease the comparison between the two systems, the same rescaling procedure as for Fig 4.3 was applied to the uniform model, only this time the scaling was chosen so that the two clusters have comparable densities after the bounce. Lengths were multiplied by 4; the time-axis is then scaled up by a factor $(4)^{3/2} = 8$. The result can be seen in panel (e); panel (f) shows a smoothed and zoomed in Hubble model for comparison.

We compare the values of the different half-mass radii of the various population before the dynamical mass segregation sets in. This process is clearly visible as the drop of the half-mass radius of the most massive stars during the evolution. We are interested in the segregation which originates from the collapse and is present before this dynamical evolution. Table 4.2 sums up the values of the half-mass radii taken at $t \sim 5$ for both models, both corresponding to the same unevolved post-collapse state (see arrows on panels e and f on Fig 4.4). With on the order of ~ 100 stars per bin or more, one estimates roughly a ten-percent standard deviation from random sampling. To measure the *relative* segregation between populations, the table also lists the ratios of each half-mass radius to the one for the most massive stars.

Both models appear mass segregated (since these ratios are significantly greater than unity). The Hubble model is more segregated, on the whole, albeit in a different way compared to the uniform model. The segregation in that one is more regular and spreads over more mass bins. In the Hubble model, the segregation is much enhanced for the first two mass bins. Such differences in the degree and nature of segregation can be explained by the clumps structure before the collapse. We showed in section 3.3.3 the clumps were mass segregated with the most massive members being preferentially located at their center. The low membership and mass of most clumps implies that segregation mostly affects the very top of the stellar mass function. This segregation, predominant among massive stars, is then found in the resulting centrally concentrated system, after the collapse, and visible on Fig. 4.4.

The inheritance of mass segregation was studied by McMillan, Vesperini & Portegies Zwart (2007) for the case of merging Plummer spheres. Allison et al. (2010) furthermore showed that mass segregation in the system as a whole is enhanced for more filamentary fractal initial condition (lower dimension, D ; see their Fig. 5). Here our results confirm this observation. Mass

segregation is a sensitive function of the initial clumpiness of the system and has immediate bearing on the dynamics of the virialised configuration, since all massive stars are more concentrated in the core.

4.4 Concluding remarks

We followed Hubble-Lemaître fragmented models throughout collapse and subsequent dynamical evolution, and compared their structure and mass segregation to cold uniform models.

Fragmented models undergo a softer, shallower collapse than uniform models, due to their irregular spatial distribution and internal kinetic energy. Uniform models eject more than twice as much stars from the system at the bounce due to this deeper collapse and virialize with a 4 times smaller half-mass radius. This high concentration enhances two-body evolution and the system expands faster than the Hubble models, even when excluding the ejected stars from the system. Interestingly, after 40 H.u, or 6 Myr, both systems achieve approximately the same density and distribution.

Both uniform and fragmented models develop mass-segregation over time, with the low-mass stars being preferentially ejected or diluted. However, just after collapse, Hubble-Lemaître models exhibit a mass segregation mainly affecting the most massive stars. This characteristic is preserved throughout evolution while the segregation seen in uniform models is more spread out in the mass function. This is a signature of the hierarchical formation, as this "Top-focused" segregation developed in small clumps and was inherited by the whole system. This would enhance colour gradient in the core of real clusters, opening the way for an observational criteria to assess the formation scenario of relaxed clusters.

